

Thermal Waves in Irradiated Protoplanetary Disks

Sei-ichiro Watanabe¹

*Department of Earth and Planetary Sciences, Nagoya University, Chikusa, Nagoya
464-8601, Japan*

seicoro@eps.nagoya-u.ac.jp

and

D. N. C. Lin²

UCO/Lick Observatory, University of California, Santa Cruz, CA 95064

lin@ucolick.org

ABSTRACT

Protoplanetary disks are mainly heated by radiation from the central star. Since the incident stellar flux at any radius is sensitive to the disk structure near that location, an unstable feedback may be present. Previous investigations show that the disk would be stable to finite-amplitude temperature perturbations if the vertical height of optical surface is everywhere directly proportional to the gas scale height and if the intercepted fraction of stellar radiation is determined from the local grazing angle. We show that these assumptions may not be generally applicable. Instead, we calculate the quasi-static thermal evolution of irradiated disks by directly integrating the global optical depths to determine the optical surface and the total emitting area-filling factor of surface dust. We show that, in disks with modest mass accretion rates, thermal waves are spontaneously and continually excited in the outer disk, propagate inward through the planet-forming domains, and dissipated at small radii where viscous dissipation is dominant. This state is quasi-periodic over several thermal timescales and its pattern does not depend on the details of the opacity law. The viscous dissipation resulting from higher mass accretion stabilizes this instability such that an approximately steady state is realized throughout the disk. In passive protostellar disks, especially transitional disks, these waves induce significant episodic

¹Visiting Researcher, UCO/Lick Observatory, University of California, Santa Cruz, CA 95064

²KIAA, Peking University, Beijing 100871, China

changes in SEDs, on the time scales of years to decades, because the midplane temperatures can vary by a factor of two between the exposed and shadowed regions. The transitory peaks and troughs in the potential vorticity distribution may also lead to baroclinic instability and excite turbulence in the planet-forming regions.

Subject headings: accretion, accretion disks — circumstellar matter — instabilities — planetary systems: protoplanetary disks — stars: pre-main-sequence — solar system: formation

1. Introduction

It has become widely accepted that dusty protoplanetary disks are heated by radiation from the central star, and that this heating mainly determines the physical structure of the outer regions of these disks. Observed infrared spectral energy distributions (SEDs) of the T Tauri disks imply that their effective temperatures T decreases with disk radius r more slowly than $T \propto r^{-3/4}$. This temperature distributions is usually explained by a model in which the thermal structure of the disk is assumed to be geometrically flared, i.e., the surface height z_s where stellar radiation is absorbed curves away from the midplane (or equivalently $z_s/r \propto r^\gamma$, with $\gamma > 0$) (Adams, Lada, & Shu 1987).

The outer regions of these disks are irradiated by the central star (Kenyon & Hartmann 1987) and the flaring enables the disks to absorb more radiation from the central star. In a steady state, the flaring index γ of a purely irradiated optically-thick disk can be obtained from the balance between intercepted stellar flux F_s incident on the surface at a low angle θ and emitted blackbody flux from the disk interior, under the assumptions that 1) the surface height z_s is everywhere proportional to the vertical gas scale height h , 2) the intercepted fraction of stellar radiation is the sine of the local grazing angle ($F_s \propto \sin \theta$), and 3) the central star is a point source. Under these circumstances, there is a self-consistent power-law solution with $\gamma = 2/7$, which corresponds to $T \propto r^{-3/7}$ (Kusaka et al. 1970; Chiang & Goldreich 1997).

In addition to this particular power-law solution, there exists an one-parameter family of solutions for the disk structure, including the diverging aspect-ratio solutions and the asymptotically conical (in which $z_s \propto r$) solutions (Dullemond 2000). Small variations in the values of z_s at inner radii where the integration starts can cause large differences in the disk structure at large radii. Dullemond (2000) speculated that such a sensitive nature of the steady solutions is suggestive to an intrinsic instability which must be analyzed with

time-dependent governing equations.

More realistic steady solutions can be obtained numerically or semi-analytically to take into account the effects of the finite values of stellar radius, the disk optical depth, and the viscous dissipation associated with the mass-accretion flow (e.g., Chiang & Goldreich 1997; Chiang et al. 2001; Dullemond et al. 2001; Tanaka et al. 2005; D’Alessio et al. 2006; Garaud & Lin 2007). The most important novel feature of these series of second-generation models is the assumed presence of superheated surface dust layers above and below the disk midplane (Chiang & Goldreich 1997). Grains in these layers are directly exposed to the stellar flux. Grains much smaller than the peak wavelength of the self emission are superheated because of their low emissivity. The disk interior is heated by the superheated dust of the layers rather than directly by the central star.

The two-layer disk model clearly explain the silicate and water-ice emission bands in observed SEDs of Herbig Ae/Be stars and T Tauri stars (Chiang et al. 2001). But, in spite of their triumph in the modeling of the observed SEDs, these models¹ are based on the assumption that z_s is proportional to the gas scale height h , with a fixed constant of proportionality $\chi = z_s/h = 4$ (Chiang et al. 2001). While this assumption has been justified by estimates which suggest that changes of χ is small throughout the disk, the amount of dust in the superheated layer is very sensitive function of χ . This dependence arises because the dust spatial density at $z_s = \chi h$ is proportional to $\exp[-\chi^2/2]$. Thus, the fixed- χ assumption may cause large discrepancy in determined values of z_s .

In previous analyses, the magnitude F_s is directly determined from the grazing angle θ (Chiang et al. 2001). This approximation justified only in the case that the length of absorption layer (say, where the optical depth to the starlight changes from 0.1 to 1) along the starlight is smaller than the lengths of radial variations of surface density or temperature. This condition would not be satisfied if the disk surface contains fluctuations resulting from the growth of short-wavelength perturbations (see § 2).

In principle, z_s is determined by the condition that the visual optical depth, which can be obtained by a direct integration along the rays of starlight, is unity and the surface filling factor A_s of the irradiated dust grains can be calculated through the vertical (in the direction normal to the disk plane) integration of geometrical opacity times mass density from z_s to infinity. This global procedure yields z_s at any given radius which depends not only on the local value of h but also the disk structure interior to that radius. Thus, $\chi = z_s/h$

¹Some author (e.g., Dullemond et al. 2001; Tanaka et al. 2005; Garaud & Lin 2007) determined χ self-consistently, but these calculations are based on the grazing-angle approximation and the assumption that χ changes slowly with radius.

varies both in space and time. Following this procedure, we can check for self consistency by recalculating z_s based on the temperature distribution obtained from the steady, constant- χ model. With this inductive approach, we demonstrate that there are substantial differences between the iterated values of z_s and the initial, assumed values of χh . We also find that A_s calculated from the deduced values of z_s is substantially different from the values of $\sin \theta$ extrapolated from the constant- χ model.

Since the irradiation heating can play such a major role in determining the vertical structure of protoplanetary disks, it is important to investigate the stability of such disks against the excitation of ripples on their surfaces. Under the assumption that the thermal timescale is much longer than the dynamical timescale in protostellar disks, D’Alessio et al. (1999) investigated the thermal stability of the irradiation-dominated disks, using a simple cooling equation. They found the vertically isothermal disk to be stable against finite amplitude perturbations. The initial temperature perturbations propagate inward and damp out quickly. However, in their analysis, they assumed that χ is constant throughout the disk and F_s is given by θ as in the grazing angle approximation. The inferred stability in that study may depend on these assumptions. As we will see in § 2, changes in χ may lead to an instability.

With a linear perturbation analysis, Dullemond (2000) showed that the flaring disk solution may become unstable to infinitesimal hydrodynamic perturbations when the cooling time of the disk is much shorter than the dynamical time (the opposite limit of D’Alessio et al. 1999). The amplitude of inwardly propagating waves grows exponentially with a rate that is a decreasing function of the wavelength. Subsequently, Dullemond & Dominik (2004a) constructed a series of numerical models to examine the two-dimensional structure and evolution of protoplanetary disks around Herbig Ae/Be stars. In these simulations, they studied the radiative transfer process under the assumption that the disk always maintains a hydrostatic equilibrium. (This assumption would not be appropriate for the limit that the time scale of cooling is shorter than that of dynamics.) They found two sets of asymptotically steady-state results which include the monotonically flaring solutions and the self-shadowed solutions. For the second set of solutions, the disk has a puffed-up inner rim. They stated that their iteration procedure, in which the hydrostatic equilibrium and the radiative transfer are treated separately in alternate steps, may not, under some circumstances, lead to a set of converged solutions. In their simulations, some wave-like disturbances appear to propagate over the disk from one iterative step to the next and these transitory features are never damped out completely. Although they limited their presentations on disks around Herbig Ae/Be stars, where the perturbation on the disk structure by these waves are relatively minor, they revealed that this problem appears to be more serious for disks around T Tauri stars. We speculate that this perturbation may be related to the above-mentioned

instabilities operating in the irradiation-dominated outer regions of protostellar disks.

In this paper, we attempt to address two issues: 1) Are the steady-state solutions of irradiated disks constructed by the previous one-dimensional models self-consistent and stable? 2) Do these regions of disks tend to undergo quasi-periodic oscillations rather than attain an asymptotic steady state? In principle, these questions should be addressed with comprehensive two- or three-dimensional numerical simulations. Such an approach is, however, fairly complicated, time consuming, and often plagued with problems in the algorithm which implements the radiative transfer processes (e.g., Dullemond & Dominik 2004a). Prior to these detailed simulations, it is useful to identify the dominant effects which regulate the dynamics of irradiated disks with a set of one-dimensional time-dependent analyses on the thermal evolution of protostellar disks.

Since thermal timescale is much shorter than viscous diffusion timescale, most previous studies adopted the assumption of thermal equilibrium during the course of disks' global evolution. Nevertheless, there have been a few investigations on the thermal evolution of protoplanetary disks. Watanabe et al. (1990) investigated the cooling and quasi-static contraction of the protoplanetary disks from an initial high-temperature state. They performed vertical one-dimensional numerical calculations and found that the cooling times are well estimated by a simple two-temperature (surface and interior temperatures) prescription. In this paper, we utilize this two-layer disk-temperature prescription to examine the stability and thermal evolution of irradiated disks.

The simplest treatments for the thermal evolution of the irradiated disk are radial one-dimensional models in which the vertical structure of the disk at each radii is analyzed independently. In order to take into account of the irradiated surface and the disk interior, we evaluate the surface height directly from the location where the visual optical depth along the straight lines from the star is unity. We show that such disks evolve to quasi-periodic states in which thermal waves propagate inward through intermediate disk radii, where planets are formed.

A simple discussion about the nature of thermal instability is given in § 2. The basic assumption of our model and its governing equations are presented in § 3. The results of our numerical calculations are presented in § 4 for both simple and realistic opacities. Finally, we summarize our findings and discuss some possible evolutionary scenarios.

2. Simple discussion about thermal instability

In this section, we discuss some potential causes for irradiation-dominated regions of disks to become thermally unstable. For illustration convenience, we adopt the following simplifying assumptions: 1) the star is a point source, 2) the disk’s internal heat sources such as turbulent viscous heating as well as external heating other than the stellar radiation are negligible, 3) the optical depth of the disk is much larger than unity for both stellar radiation and its own emission, and 4) the transport of energy in the radial direction is much smaller than that in the vertical direction. Note that these assumptions are adopted only in this section for the purpose of pinpointing the physical process which leads to the thermal instability. All of these idealized assumptions will be relaxed in the numerical simulations to be presented below.

Under these assumptions, we consider the heat balance in a geometrically thin disk which is irradiated by the central star. The energy equation reduces to

$$C\Sigma\frac{\partial T_{\text{m}}}{\partial t} = 2(F_{\text{s}} - F_{\text{m}}), \quad (1)$$

where C is the specific heat per unit disk mass, Σ is the surface density of the disk, and T_{m} is the temperature of the disk interior. Under assumption 2, the disk interior has an approximately isothermal structure and F_{m} is the disk blackbody emission given by

$$F_{\text{m}} = \sigma T_{\text{m}}^4, \quad (2)$$

and F_{s} is the intercepted stellar flux given by

$$F_{\text{s}} = \frac{1}{2} \frac{L_{\star}}{4\pi r^2} A_{\text{s}}, \quad (3)$$

where σ is the Stefan-Boltzmann constant, L_{\star} is the stellar luminosity, r is the cylindrical radial coordinate, and A_{s} is the total emitting area-filling factor of superheated dust grains. The factor 1/2 in the right-hand side of equation (3) comes from the fact that surface irradiated dust re-radiate half of the absorbed stellar flux toward the disk interior (the rest toward infinity). Assuming a homogeneous mixing of gas and dust, we can obtain A_{s} from (see Appendix C)

$$A_{\text{s}} = \tau_{\text{G}} \operatorname{erfc}\left(\frac{z_{\text{s}}}{\sqrt{2}h}\right) = \tau_{\text{G}} \operatorname{erfc}\left(\frac{\chi}{\sqrt{2}}\right), \quad (4)$$

where $\operatorname{erfc}(x)$ is the complimentary error function, τ_{G} is the geometrical optical depth of the disk midplane, and z_{s} is the surface height where stellar radiation is absorbed. The ratio of the surface height z_{s} to the gas scale height h is denoted by $\chi \equiv z_{\text{s}}/h$. In a hydrostatic

equilibrium, the gas scale height h is given by

$$h = \frac{c_m}{\Omega_K} = \left(\frac{k_B T_m r^3}{\mu m_u G M_\star} \right)^{1/2}, \quad (5)$$

where c_m is the disk sound speed, Ω_K is the Keplerian angular velocity, k_B is the Boltzmann constant, μ is the molecular weight of disk gas, m_u is the atomic mass unit, G is the gravitational constant, and M_\star is the stellar mass.

Figure 1 displays the F_m and F_s (at 10 AU) as functions of T_m . Assuming that the initial state is in a thermal equilibrium (corresponding to the point where three thick lines cross) with $T_m = T_{m,\text{eq}}$, we impose a small positive temperature perturbation. We consider two extreme cases: 1) If z_s is determined by the local disk structure, $\chi = z_s/h$ would retain a constant value during the increase of T_m such that A_s would also be constant (see eq. [4]) and F_s would not change (*dot-dashed line*). In this case the system would be stabilized because $F_m > F_s$ for $T_m > T_{m,\text{eq}}$. 2) If z_s is determined mostly by the attenuation by dust in the inner regions of the disk, z_s would remain constant despite changes in the local disk temperature and h such that A_s would increase rapidly and F_s would increase much faster than F_m (*thick dash curve*). In this case the system would be unstable because $F_m < F_s$ for $T_m > T_{m,\text{eq}}$.

In their stability analysis, D’Alessio et al. (1999) assumed a constant χ . Based on the above analysis, this assumption naturally leads to stable solutions. In fact, most of the analysis on the structure of irradiated disks are based on the constant- χ assumption (e.g., Chiang et al. 2001). The usual procedure to determine z_s is based on a geometrical consideration, i.e,

$$A_s = \sin \theta \simeq \frac{z_s}{r} \left(\frac{d \ln z_s}{d \ln r} - 1 \right), \quad (6)$$

where θ is the grazing angle (i.e., the angle between the starlight and the disk surface). We refer this procedure to be the grazing-angle approximation. Most previous steady-state disk models are constructed with equation (6) under the assumption that χ is constant throughout the disk.

However, the magnitude of χ is generally determined by the radial structure of the disk as well as its local properties. The surface height z_s is determined by the optical depth integrated through a ray of the stellar radiation. We derive a ray integral and check the validity of equation (6) in § 3 and Appendix C. In principle, equations (4) and (6) must be resolved simultaneously (Tanaka et al. 2005). However, this set of equations is fairly unstable to solve numerically because they do not contain contributions which may reduce any steep temperature gradients in the radial direction.

Step temperature gradient, if present, would invalidate the constant χ and the grazing-angle approximations. Physically, the radial transport of heat suppresses the radial temper-

ature gradient, but such a process through the opaque regions of the disk must be analyzed with multi-dimensional numerical simulations. One of the most efficient process of the radial heat transport is the radiative transfer from the superheated dust grains at the surface of any radial location to the disk midplane at adjacent radial regions. Using a simple one-dimensional model, we can take this oblique radiative transfer of heat into account.

3. Basic Equations

Following the approaches of Chiang & Goldreich (1997) and Garaud & Lin (2007), we construct numerical models to study the thermal evolution of a protostellar accretion disk. The surface of the disk is illuminated by the central star. Exposed to the stellar radiation, sub-mm dust grains in the surface layers of the disk are superheated. We consider the case that dust mass of the disk is so large that the disk midplane (except for an innermost region where silicates are evaporated) is optically thick to the stellar radiation. In contrast to the previous section, the heat sources for the disk interior in these numerical models include both irradiation from the superheated grains on the disk surface and the viscous dissipation associated with the accretion flow. We adopt a cylindrical coordinate system (r, ϕ, z) in which the $z = 0$ plane represents the disk midplane and the origin is at the location of the central star. Since the star-and-disk system is symmetric with respect to the midplane, we describe our results for the upper half of the disk only.

In order to simplify the problem we adopt the two-layer axisymmetric disk model proposed by Chiang & Goldreich (1997). In this model, the disk consists of a surface superheated layer where the dust temperature is $T_s(r)$ and a disk interior where the dust and gas temperature is assumed to be uniform at $T_m(r)$. This model is simple to use and includes all the essential ingredient to analyze the onset, evolution, and stabilization of thermal instability in protostellar disks. However, such a simplification would be invalid if the disk optical depth $\tau_m(T_m)$ to its intrinsic radiation is much larger than unity and viscous heating rate is larger than surface heating rate. However, the dust optical depth may be self-limited by their rapid growth through cohesive collisions, so that $\tau_m(T_m) \lesssim 10$ throughout the disk (see Fig. 6 in Tanaka et al. 2005). Thus, the two-layer model is valid even in the inner disk where dust surface density is larger.

The two-layer model is invalid at the inner edge of the disk, where disk is irradiated not only from the top but from the radial direction. The disk may have a puffed-up inner rim (e.g., Dullemond & Dominik 2004a), but a set of two-dimensional radiative transfer calculations is needed to determine the structure of the innermost region. In this work we simply assume that disk within 0.1 AU is optically thick in the radial direction and has no

puffed-up rim that might cast shadows over the outer regions of the disk. We confine our calculations only in the regions $r > 0.1$ AU, where the two-layer model is valid.

The thermal timescale of the disk interior at radius r is given by (see eq. [12])

$$\begin{aligned} t_{\text{th}} &= \frac{(\gamma_a + 1) c_m^2 \Sigma}{2(\gamma_a - 1) \sigma T_m^4} \\ &\simeq 53 \left(\frac{\Sigma_0}{\Sigma_{\text{H}0}} \right) \left(\frac{T_{\text{m}0}}{124 \text{ K}} \right)^{-3} \left(\frac{r}{1 \text{ AU}} \right)^{3q-p} \text{ yr}, \end{aligned} \quad (7)$$

where γ_a is the adiabatic exponents and c_m is the sound speed of the disk interior. For evaluation, we assume here power-law distributions for the total (gas + dust) surface density $\Sigma(r) \propto r^{-p}$ and the midplane temperature $T_m(r) \propto r^{-q}$. The normalization factors, Σ_0 and $T_{\text{m}0}$, refer to their corresponding values at $r = 1$ AU. The nominal value of surface density is given by that in the minimum mass solar-nebula (MMSN) model in which $\Sigma_{\text{H}} = 1.7 \times 10^3 \text{ g cm}^{-2}$ (Hayashi 1981).

We assume that the thermal timescale t_{th} to be much longer than the dynamical time (Ω_{K}^{-1}), but much shorter than the viscous evolution time (r^2/ν , where ν is the turbulent viscosity). In this case we can regard that the whole region of the disk is always in a hydrostatic equilibrium in the vertical direction and has time-independent surface densities.

The temperature T_s of superheated dust grains is given by

$$\frac{L_{\star}}{4\pi r^2} = 4\epsilon_s \sigma T_s^4, \quad (8)$$

where ϵ_s is the averaged emissivity of the dust grains at T_s . Along a ray from the surface of the star, the superheated layer extends outward until the position where visual optical depth has reached unity. We take into account the attenuation of the stellar photons by defining the height z_s of the bottom of the superheated layer with the following equation

$$\tau_s(T_{\star}; r, z_s(r)) = 1. \quad (9)$$

Here $\tau_s(T_{\star}; r, z)$ is the optical depth between the central star and the point (r, z) to the blackbody radiation peaked at the stellar effective temperature T_{\star} , given by the following integration

$$\tau_s(T_{\star}; r, z) = \int_{R_{\star}}^r \bar{\kappa}_s(T_{\star}) \rho_d(r', \zeta r') (1 + \zeta^2)^{1/2} dr' \quad (10)$$

along a straight path from the star to the point (r, z) . Here R_{\star} is the stellar radius, $\zeta \equiv z/r$ is the aspect ratio, $\rho_d(r', z')$ is the spatial mass density of dust at (r', z') , and $\bar{\kappa}_s(T_{\text{rad}})$ is the Planck mean opacity of the grains interacting with the blackbody radiation peaked at T_{rad} .

Note that we define here the grain opacity per unit *dust mass*, not per unit total (gas + dust) mass as in the usual definition, because it is convenient for the consideration of the case that the dust-to-gas ratio may change vertically. The emissivity in equation (8) can be given by

$$\epsilon_s = \frac{\bar{\kappa}_s(T_s)}{\bar{\kappa}_s(T_\star)}. \quad (11)$$

The energy equation includes heating from both stellar irradiation and viscous dissipation as well as radiative losses from the disk surface such that (see, e.g., Watanabe et al. 1990)

$$\frac{(\gamma_a + 1) k_B \Sigma}{2(\gamma_a - 1) \mu m_u} \frac{\partial T_m}{\partial t} = 2 [F_s - F_m] + \frac{3}{4\pi} \dot{M} \Omega_K^2, \quad (12)$$

where \dot{M} is the mass accretion rate, which we assume to be constant throughout the disk. Note that the steady state assumption is compatible with a power-law surface density distribution for some effective viscosity prescriptions (Chiang & Goldreich 1997; D’Alessio et al. 2006; Garaud & Lin 2007).

Further, F_s and F_m are, respectively, the thermal radiation fluxes downward from the superheated dust grains high up in the disk atmosphere and upward from dust grains in the disk interior,

$$F_s(r) = [1 - e^{-2\tau_m(T_s)}] \frac{L_\star}{8\pi} \left\langle \frac{A_s}{r^2} + \frac{4R_\star}{3\pi r^3} \right\rangle, \quad (13)$$

$$F_m(r) = [1 - e^{-2\tau_m(T_m)}] \sigma T_m^4, \quad (14)$$

where $\tau_m(T_s)$ and $\tau_m(T_m)$ are the optical depths of the disk interior (from $z = 0$ to $z = z_s$) to the radiation from the superheated dust grains and to its own emission, respectively, and A_s is the total emitting-area filling-factor of superheated dust grains. We consider the effect of finite radius of the central star in F_s , which is important in the inner part of the disk. We also consider the effects of oblique radiative transfer: the angular brackets in the right-hand side of equation (13) represent radial averaging of radiation emitting from superheated dust within the adjacent regions (see § 4). The factors 2 in the exponential functions in equations (13) and (14) also denote oblique radiative transfer in the disk interior (Tanaka et al. 2005).

Once the dust density distribution $\rho_d(r, z)$ of the disk is specified, A_s and τ_m can be determined from the following integration:

$$A_s(r) = 1 - \exp \left[- \int_{z_s(r)}^{\infty} \tilde{\kappa}_s(T_\star) \rho_d(r, z') dz' \right], \quad (15)$$

$$\tau_m(T_{\text{rad}}; r) = \int_0^{z_s(r)} \bar{\kappa}_m(T_{\text{rad}}) \rho_d(r, z') dz', \quad (16)$$

where $\bar{\kappa}_m(T_{\text{rad}})$ is the Planck mean opacity of midplane grains interacting the blackbody radiation peaked at temperature T_{rad} . Further details of dust opacity are shown in §4 and Appendix A.

We assume that the total (gas+dust) surface density Σ of the disk is a simple power-law distribution in the radial direction:

$$\Sigma = \Sigma_0 \left(\frac{r}{r_0} \right)^{-p}, \quad (17)$$

which is kept constant during the thermal evolution considered in this work.

Taking the effects of dust settling, we can obtain dust density distribution ρ_d of the disk in the two-temperature model adopted here (see Appendix B). However, computationally intense iterative calculation is needed to determine, self-consistently, the magnitudes of ρ_d and z_s simultaneously. Instead of equations (B4) and (B6), we adopt, in most of the calculations, the following simple density distribution for the dust:

$$\rho_d(r, z) = \frac{\Sigma_d}{\sqrt{2\pi}h} \exp\left(-\frac{z^2}{2h^2}\right), \quad (18)$$

where Σ_d is the surface density of dust. We put $\Sigma_d = f_d \Sigma$, where f_d is the dust fraction in the surface density. We dub f_d the dust-to-gas ratio. In the disk interior, dust sedimentation is not so important unless the radii of dust are not so large that we can formally set the dust density distribution to be equation (18). In the surface layer, dust settling reduces the dust density while high surface temperature T_s raise it, so that equation (18) also gives a good estimate. In some cases we compared results with more realistic dust distribution given in Appendix B and found that they are very similar unless dust sizes are not so large. We discuss the difference of the results between the two distributions in § 5.

We found that if the gradient $d \ln z_s / d \ln r$ changes rapidly in r direction, the approximation used to derive equation (6) is no longer justified (see Appendix C). For this reason we use equations (9) and (15) instead of equation (6).

4. Numerical Results

We adopt the following values as fixed parameters for all models: the mass, radius, and luminosity of the central star are set to be $M_\star = 1M_\odot$, $R_\star = 2.085R_\odot$, and $L_\star = 1L_\odot$, respectively, so that its effective temperature is $T_\star = 4000$ K. For the disk gas, we specify $\mu = 2.34$ and $\gamma_a = 1.4$.

We adopted the phenomenological MMSN model (Hayashi 1981) for the standard gas and dust surface density distribution. In this model, $\Sigma_0 = \Sigma_{\text{H0}} = 1.7 \times 10^3 \text{ g cm}^{-2}$ with $r_0 = 1 \text{ AU}$ and $p = 1.5$ in equation (17). For comparison, we also calculate a relatively flat Σ distribution with $p = 1.0$ and $\Sigma_0 = 3.54 \times 10^2 \text{ g cm}^{-2}$. These surface densities are kept constant with time. The dust-to-gas ratio f_d and solid material density ρ_{mat} are set to be 0.014 and 1.4 g cm^{-3} , respectively. In § 4.1 we neglect any changes of dust surface density due to sublimation and use the value of f_d throughout the disk. In § 4.2 we consider the effect of ice sublimation. We also vary the mass accretion rate from $\dot{M} = 0$ to $10^{-7} M_{\odot} \text{ yr}^{-1}$. These steady-state accretion rates are consistent with our specified surface density and temperature distributions provided the magnitude of α is a function of the radius, where α is the non-dimensional turbulent viscosity in the so-called α -prescription (Shakura & Sunyaev 1973).

The normalization time unit is the thermal timescale given by equation (7) with $\Sigma = \Sigma_0$ and $T_m = T_{m0}$. We denote the time unit as $t_{\text{th},0}$ and the non-dimensional time as $\hat{t} = t/t_{\text{th},0}$. For the standard model, we set the magnitude of $\Sigma_0 = \Sigma_{\text{H0}}$ and $T_0 = 124 \text{ K}$, so that $t_{\text{th},0} = 53 \text{ yr}$. Note that the local thermal timescale t_{th} is nearly constant with r in the standard disk model with $p = 1.5$. The non-dimensional time step used in the numerical integration is set to be $\delta\hat{t} = 0.005$. In order to verify numerical convergence, we also perform several calculations with time step half of the standard value and confirmed that the results have no significant changes.

The spatial grid consists of 90 points (the standard case) or 180 points (the high-resolution case), logarithmically distributed, between $r = 0.1 \text{ AU}$ and 100 AU . Numerical oscillation would be induced if there is no radial exchange of energy at all. At any radius, the disk interior is exposed not only to the superheated surface grains directly overhead, but also obliquely to those at adjacent radial locations. Such a radial exchange of energy tends to suppress instabilities for short-wavelength perturbations. In our numerical scheme, we assume that the isotropic radiation comes from all radius r' within $|r' - r| < z_s(r)$ contributes to the heating at radius r as expressed in equation (13). This implementation stabilizes the short wave-length oscillation and the results are essentially independent of the numerical resolution.

4.1. Constant Opacity

In this subsection, we first illustrate the dominant features using a simple opacity model. We adopt the emissivity and opacity (per unit *dust mass*) of the grains interacting with

blackbody radiation peaked at temperature T_i to be

$$\epsilon_s(T_i) = \left(\frac{T_i}{T_\star}\right)^\beta \quad \text{and} \quad \bar{\kappa}_s(T_i) = \bar{\kappa}_{s0} \left(\frac{T_i}{T_\star}\right)^\beta, \quad (19)$$

where we choose the value of $\bar{\kappa}_{s0} = 10^2 \text{ cm}^2 \text{ g}^{-1}$, which approximately corresponds to the commonly defined opacity per unit *gas mass* with the value of $1 \text{ cm}^2 \text{ g}^{-1}$. Most of the calculation shown here is for $\beta = 0$ but we also calculate some models with $\beta = 1$ for comparison purposes.

For initial conditions, we adopt the steady state solution obtained from the time integration with fixing $\chi(r)$. This set of initial conditions does not correspond to the asymptotic steady-state solutions because the initial estimate of χ is not self-consistently compatible with the actual aspect ratio ζ_s of the surface. Nevertheless, the numerical calculations relax to nearby steady solutions if they exist. In order to verify that our results are independent of the adopted initial conditions, we calculate the evolution of the disk with several different initial guesses for χ and found that the system reaches to the same asymptotic state.

We first show the results of the calculations with no mass accretion ($\dot{M} = 0$). Figure 2 shows the initial evolution of the midplane temperature T_m as well as the surface temperature T_s , which is kept constant with time. The elapsed time is $\hat{t} = 1.6$, i.e., $t = 1.6t_{\text{th},0} \simeq 85 \text{ yr}$ and each curve corresponds to a time step $\Delta\hat{t} = 0.2$ ($\Delta t = 10.6 \text{ yr}$). At first, the initial state is almost stable in the innermost region and the outermost region. But, in the intermediate regions (0.5–20 AU), the disk becomes unstable. At a typical instance of time, four local temperature peaks (high T_m and z_s) coexist and are amplified. These peaks move inward (toward the star) as they grow. Hence, we refer these propagating perturbations as waves. During the amplification of the waves, they cast shadows over the outer regions of the peak. The temperature T_m decreases in the shadowed regions. Each fully-grown wave has a sharp slope on the inner ‘exposed side’ of the peak and a gentler decline on the outer ‘shadow side’. The waves propagate inward with velocities about a few tenth of r/t_{th} . The outermost wave ($\sim 16 \text{ AU}$) begins to grow just outside the shadowed region of the inner adjacent wave when the shadowed region is developed. This tendency shows that the outermost wave may be induced by the wave ahead of it.

Additional time integration shows that as these waves propagate inward they begin to decay when they reach inside 1 AU. The waves are completely damped out at around 0.25 AU. In contrast, new waves are formed continually at the outermost region ($> 20 \text{ AU}$) of the computational domain. The growth region of waves gradually retreats and the maximum amplitude of each wave during its propagation cycle gradually increases with time. The system reaches a quasi-periodic state when $\hat{t} \sim 8$. Figure 3 shows the evolution of T_m at this stage. Waves are continuously formed and amplified at the outer disk ($> 30 \text{ AU}$), then prop-

agate inward with nearly constant amplitude through the intermediate disk regions, begin to decay at about 1 AU, and are damped out completely at around 0.25 AU. Temperature in the innermost disk region ($r < 0.25$ AU) attains steady values. The propagation speed of the waves is approximately given by r/t_{th} . In the intermediate disk radii (1–20 AU), the peak temperature of each wave is 2–3 times higher than the bottom temperature in the inner adjacent shadowed region.

The radial profile of each wave is somewhat skewed. The half width of individual waves is about 0.1–0.2 r on the inner side and 0.2–0.4 r on the outer side. The wavelength is approximately twice as large as $z_s(r)$. Due to the steep radial temperature gradient, the magnitude of $z_s(r)$ is affected by the variation in the thickness h at the disk regions interior to r on this length scale. The ratio of the radii between two adjacent wave peaks are about 20 if both waves are within $r > 1$ AU. Near the inner boundary of the propagating-wave zone, the finite size of the star (R_*) becomes comparable to the surface height z_s . This time-independent contribution in equation (13) essentially stabilizes the innermost region of the disk.

The change of other variables at the same epoch as Figure 3 are shown in Figures 4–8. Figure 4 shows the time evolution of $\zeta_s = z_s/r$. Outside 0.25 AU, ζ_s changes stepwise. The two or three step jumps of ζ_s correspond to the leading inner side of the thermal waves. The magnitude of increase in z_s at the leading edge of each step reaches a maximum of 1.5 around 10 AU. The flat portions of ζ_s correspond to the shadowed regions, where ζ_s is determined by the stellar ray which passes above the peak of each wave.

Figure 5 shows the time evolution of $\chi = z_s/h = \zeta_s/\zeta_h$. The local minima of χ are located just ahead of the peaks in T_m . The decrease of χ is essential for the temperature raise. In the shadowed regions χ increases because ζ_s is kept almost constant (see Fig. 4), whereas $\zeta_h = h/r$ decreases. Changes in the value of χ produces the variations in the surface filling factor A_s . The time evolution of A_s is shown Fig. 6. Sharp peaks of A_s , which correspond to the minima of χ (see eq. [C1]), propagate inward. Note that the variation in the amplitude of A_s is very large, ranging from a few tenth at the peaks to below 10^{-3} in the shadowed region. Such large changes of A_s induce rapid heating in front of the waves and rapid cooling in the shadowed regions. The unperturbed z_s in the intermediate regions is comparable to the half width of the propagating waves. Modest variations in χ can lead to nonlinear dissipation, such that the wave amplitudes are also limited in these region.

We also plot the evolution of the distribution of the logarithmic pressure gradient $d\ln P/d\ln r$ (Fig. 7), where $P(r)$ is the pressure in the midplane of the disk. This plot indicates that the gas pressure gradient is nearly reversed just in front of the peak of the waves. This inversion occurs due to the steep positive temperature gradient in the exposed,

leading, inner face of the waves. Consequently, the velocity of the gas departs significantly from its unperturbed sub-Keplerian values. In a follow-up paper, we will consider the associated gas drag on grains of various sizes. Another interesting quantity is the distribution of the potential vorticity (or vortensity):

$$\frac{\Omega_{\text{ep}}}{\Sigma} = \frac{1}{\Sigma r^3} \frac{d}{dr} r^4 \Omega^2, \quad (20)$$

where Ω_{ep} is the epicyclic frequency and Ω is the angular velocity of gas. Note that in a quasi-Keplerian disk $\Omega_{\text{ep}} \simeq \Omega_{\text{K}} \propto r^{-1.5}$, so that the potential vorticity is almost constant for MMSN with $p = 1.5$. The thermal waves disturb the potential vorticity through the change of pressure gradient. Figure 8 displays the evolution of the distribution of the potential vorticity. There are peaks and troughs around the waves. Local extrema of this quantity can lead baroclinic instabilities which may excite turbulence (e.g. Klahr & Bodenheimer 2003) in the dead zone where the magneto-rotational instability may have limited influences (Gammie 1996). Further investigation of this possibility will also be considered elsewhere.

Next, we examine the dependence of wave excitation and propagation on the mass accretion rate (\dot{M}). Other than the value of \dot{M} in the energy equation, we adopt the same model parameters as for the no-accretion case shown in Figures 2–8. Thus, in the present context, the primary physical effects associated with the accretion flow is the viscous dissipation. This internal energy source (viscous dissipation) in equation (12) has a greater fractional contribution to the energy budget in the inner regions than the outer regions of the disk (Garaud & Lin 2007).

Although quasi-periodic oscillations are excited in all cases, the radial extent where they propagate to depends on the magnitude of \dot{M} . Figure 9 shows the time evolution of T_{m} in a quasi-periodic state for the case of $\dot{M} = 10^{-8} M_{\odot} \text{yr}^{-1}$. The result is similar to that obtained by neglecting the viscous dissipation. In this case, waves are excited in the outer region, propagate inward and are damped out in the innermost region. In comparison with the no-accretion model, the innermost region in this case is hotter ($T_{\text{m}}(0.1 \text{ AU}) \sim 600 \text{ K}$) with larger thickness. The *time-independent* contribution of viscous heating to the energy equation provides a stabilizing effect to a slightly larger radial extent ($r < 0.5 \text{ AU}$) compared with the no-accretion case ($T_{\text{m}}(0.1 \text{ AU}) \sim 500 \text{ K}$ and $r < 0.25 \text{ AU}$).

The quasi-periodic state, however, is drastically changed in the $\dot{M} = 1 \times 10^{-7} M_{\odot} \text{yr}^{-1}$ model (Fig. 10). The disk becomes stable interior to about 6 AU. In the outer region, there are two high-temperature peaks, both oscillate quasi-periodically. The positions of the two peaks do not coherently propagate inward as in the case of $\dot{M} = 1 \times 10^{-8} M_{\odot} \text{yr}^{-1}$, but they fluctuate to and fro around 12 AU and 40 AU, respectively. The ranges of temporal temperature changes are less than 2 K over the disk, so that the disk is regarded to be in

an approximately steady state. This result shows that the disk becomes stabilized as \dot{M} increases.

Finally, we show the dependence on the disk surface density Σ . Note that Σ affects the evolution not only through the optical depth of the surface layer but through the thermal timescale. We perform several calculations for $\Sigma_0 = 3.54 \times 10^2 \text{ g cm}^{-2}$ and $p = 1.0$. Note that the time unit for this case is $t_{\text{th},0} = 11.0 \text{ yr}$. We calculate the disk evolution for this surface density distribution with several values of \dot{M} and find that the results are quite similar to the case with the standard surface density distribution. The quasi-periodic wave solutions are obtained for small \dot{M} , whereas the disk becomes nearly steady for large \dot{M} .

Figure 11 shows the temporal variation of T_m in the quasi-periodic state for this prescribed $\Sigma(r)$ distribution with $\dot{M} = 10^{-8} M_\odot \text{ yr}^{-1}$. Comparing to the case with $p = 1.5$ (Fig. 9), the wave propagating region is relatively narrow, confined to the regions between 1 AU and 20 AU, and the maximum amplitude of waves is also smaller. Outermost region where $r > 20 \text{ AU}$, the amplitudes of waves are limited and do not exceed about 2 K. The amplitudes grow as waves propagate from 20 AU to 8 AU, then they attain a nearly constant value from 8 AU to 1.5 AU. The waves are finally damped at 1.5–1 AU. In an analogous inviscid model (i.e., with an identically prescribed $\Sigma(r)$ distribution but without viscous dissipation), the result is quite similar to that in Figure 11 except that the wave propagating region extends slightly closer to the star. The results for the $\dot{M} = 10^{-7} M_\odot \text{ yr}^{-1}$ model show that the disk attains an approximately steady state with only very small fluctuations (amplitude is less than a few tenth K) remaining in the outermost region.

All the above results are for $\beta = 0$. We also calculate cases with $\beta = 1$. Other than a modification in the distribution of T_s and T_m , the time dependent nature of wave excitation and propagation is essentially independent of the value of β . In all cases, we find that the quasi-periodic nature of the inwardly-propagating thermal waves is realized for the disk with $\dot{M} \lesssim 10^{-8} M_\odot \text{ yr}^{-1}$. The basic features of this state do not strongly depend on other parameters such as p and β . In order to verify the universality of these results, we perform further calculations with more realistic opacities.

4.2. Realistic Opacities

In this subsection, we present the results based on models with more realistic grain-opacity prescription given by Tanaka et al. (2005). In this prescription, grains are assumed to be consisted of a uniform mixture of H₂O-ice, organics, olivine, pyroxene, metallic iron, and troilite, the abundances of which are given by Pollack et al. (1994). For relatively high

temperatures ($T > 160$ K), we use the dust opacity of grains without ice or organics. For the low-temperature ($T < 160$ K) state, the opacity includes the contribution from ice and organics grains. Based on the single-sized monochromatic opacity table made by H. Tanaka (Tanaka et al. 2005), we calculate the Planck mean of the size-averaged opacities $\bar{\kappa}_s(T_{\text{rad}})$ and $\bar{\kappa}_m(T_{\text{rad}})$ with an assumed power-law grain-size distribution $n(s) \propto s^{-3.5}$, which is truncated for a minimum and maximum range of $s_{\text{min}} = 0.1 \mu\text{m}$ and $s_{\text{max}} = 1 \text{ mm}$, respectively (see Appendix A).

For illustrative models, we adopt the standard surface-density distribution of the MMSN model. For the gas-to-dust ratio f_d , we consider two limiting cases: 1) a constant ratio $f_d = 0.014$ and 2) a ratio which includes the effect of ice sublimation. In the latter case, $f_d = 0.0043$ for $T > 160$ K and $f_d = 0.014$ for $T < 160$ K. In the actual implementation, these values are smoothly connected around the sublimation temperature by a hyperbolic tangent function. Note that even in the constant- f_d cases, the opacity undergoes a transition across $T = 160$ K.

We perform a set of calculations with this realistic opacity. Similar to the previous models with constant opacity, the disk evolves into a quasi-periodic state after about 10 times of the thermal timescale. First, we show the results for the case with a constant gas-to-dust ratio. Figure 12 shows the time evolution of T_m in the asymptotic quasi-periodic state of the disk with $\dot{M} = 1 \times 10^{-8} M_{\odot} \text{ yr}^{-1}$. The surface temperature T_s is also shown in Figure 12. From equations (8) and (11), we note that T_s is independent of time. Comparing with the constant-opacity case in which $\beta = 0$ (Fig. 9), T_s is everywhere larger for the realistic grain opacity, because of the effect of superheating. There is a small jump at the radius where opacity law changes ($T_s \simeq 160$ K). For the same value of \dot{M} , the structure of wave propagation region is very similar to that of the constant-opacity case.

With a sufficiently large mass-accretion rate ($\dot{M} = 1 \times 10^{-7} M_{\odot} \text{ yr}^{-1}$), the disk with a realistic opacity is also stabilized by the effect of viscous dissipation (Fig. 13). There are three local maxima in the T_m distribution. The innermost peak at about 6 AU corresponds to an opacity transition in the disk’s surface layer ($T_s \sim 160$ K). All these local peaks do not propagate but fluctuate quasi-periodically with a small amplitude.

Finally, we show the effect of ice sublimation. Figure 14 displays the evolution of T_m for the model in which the dust surface density is modified by the ice sublimation. Taking into account the effect of dust’s size sorting on the opacity, we assume that surface dust grains has a smaller maximum size $s_{s,\text{min}}$ than those in disk interior $s_{m,\text{min}} = s_{\text{min}} = 1 \text{ mm}$. We choose $s_{s,\text{min}} = 1 \mu\text{m}$. Owing to the increase of A_s associated with the ice condensation in surface layer, the T_m distribution attains a local maximum near 5 AU. This peak does not propagate in time. Interior to this snow line, a wave propagates to about 0.5 AU. Outside

this snow line, there is another local maximum near 20 AU, which may be induced by the emergence of the first peak. Compare to the model in which the ice sublimation is neglected (Fig. 12), the ice-condensation induces the formation of a local thermal maximum which prevents waves from emerging at large radii and propagate inward.

5. Summary and Discussion

We have performed a set of radial one-dimensional calculations to examine the thermal evolution of hydrostatic disks, using the direct integration of optical depths $\tau_s(T_*)$ to determine the optical surface z_s and total emitting area-filling factor A_s of a superheated layer. Our results suggest that, in regions with modest and steep radial temperature gradients, the constant $\chi = z_s/h$ assumption is incompatible with the computed height of the surface where $\tau_s(T_*; r, z_s) = 1$. The initial state obtained by a fixed- χ iteration evolves spontaneously to the state where thermal waves grows. The disks evolve to a quasi-periodic state where thermal waves continuously propagate toward the star in the intermediate radii.

The driving mechanism for this thermal instability is the intense stellar irradiation high up in the disk atmosphere. It is a consequence of a “shadowing effect” in which the surface where most of the stellar photons are intercepted at any given radial location may be affected by the vertical structure in the disk regions interior to that radius. This quasi-periodic state is stabilized by viscous dissipation associated with the mass accretion flow through the disk. For the cases of $\dot{M} = 10^{-7} M_\odot \text{ yr}^{-1}$ wave excitation and propagation are suppressed and the disks reach approximately steady states. In order to eliminate the possibility of artificial dependence on the initial conditions, we perform the following numerical experiments. By setting the initial condition for an approximately steady state with $\dot{M} = 10^{-7} M_\odot \text{ yr}^{-1}$ and by decreasing the mass accretion rate to $\dot{M} = 10^{-8} M_\odot \text{ yr}^{-1}$, we calculate the time evolution of the disk. We find that the system evolves to a quasi-periodic state within about 10 times of thermal timescale. The asymptotic quasi-periodic state is identical to that obtained with the standard calculation for $\dot{M} = 10^{-8} M_\odot \text{ yr}^{-1}$, which is shown in Figure 9. Inversely, we also start a calculation from a quasi-periodic state with $\dot{M} = 10^{-8} M_\odot \text{ yr}^{-1}$ and increase the mass accretion rate to $\dot{M} = 10^{-7} M_\odot \text{ yr}^{-1}$. The disk evolves into an approximately steady state, which is almost identical to that obtained with the standard calculation for $\dot{M} = 10^{-7} M_\odot \text{ yr}^{-1}$, which is shown in Figure 10. These results show that the state of the disks are determined by the instantaneous mass accretion rate (note that viscous evolution time is much longer than thermal timescale).

The result that the quasi-periodic wave-propagating states exist in disks with modest disk accretion rate is robust to variations in the disks’ structural parameters such as their

surface density profile, opacity law, and vertical dust distribution. Whereas these parameters weakly affect the positions of the inner and outer boundaries of the wave-propagating domains, they do not affect the basic features of the waves such as their amplitude and shape.

We also perform some calculations for the constant-opacity case using a general surface density profile (eq. [B6] instead of eq. [18]). The results are quite similar with that of the simple density profile. The difference is even less noticeable than that due to change of opacity law.

Using the calculated thermal structure of the disk, we obtain the disk SED. We assume that the disk is face-on and truncated both at inner 0.1 AU and outer 100 AU. Figure 15 shows the evolution of the SEDs associated with the model illustrated in Figure 14. Contribution from the central star to the SEDs is included in this figure. The SEDs are expected to oscillate periodically within mid-infrared wavelengths. This variation correspond to the periodic propagation of the thermal waves. In this case, the period of oscillation is about $t_{\text{th},0} \simeq 53 \text{ yr}$. In general this time scale varies depending on the surface density distribution and accretion rate in the disk as well as the luminosity of the central star. The change of disk SED comes from not only emission from the disk interior where T_{m} changes but also emission from the superheated surface layer where, even if T_{s} is kept constant, A_{s} would modulate. The surface emission also contributes to the water-ice and silicate emission bands. We expect the relative heights of these emission bands in SEDs to modulate with time. Note that this calculated SED is somewhat artificial because disk is truncated at the inner and outer edges. Thus, the direct comparison with observation may be meaningless. Nevertheless, the predicted relative variations of SEDs due to propagation of the thermal waves are likely to be important in the interpretation of the observed SEDs, especially those of the so-called transitional disks taken by *SPITZER* Infrared Spectrograph (IRS) (e.g., Furlan et al. 2006).

In this work, we assume t_{th} to be much longer than Ω_{K}^{-1} , so that a hydrostatic equilibrium would be quickly re-established after the passage of the thermal waves. This assumption is invalid in the outer regions (say $> 20 \text{ AU}$, see eq. [7]). But our calculations show that the wave propagating region is extended to regions interior to 1 AU. This result implies that even if dynamic effect may suppress the thermal waves in the outer disk, the waves can still be excited in the inner regions. According to previous linear analysis (Dullemond 2000), the disk becomes unstable to infinitesimal hydrodynamic perturbations when $t_{\text{th}} \ll \Omega_{\text{K}}^{-1}$. This type of instabilities may also excite the thermal waves.

The results presented here is based on simple radial one-dimensional analysis in which a two-temperature approximation is adopted to describe the vertical structure of the disk. We also neglected modulations in the surface density and accretion rate throughout the

disk. Our next task is to relax these assumptions and to generalize our results to a set of genuine two-dimensional simulations in which the radiation and mass transfer can be considered simultaneously. Since dust growth time or radial migration time are comparable to the thermal timescale, it will also be important to consider the evolution of the dust particles (e.g., Takeuchi & Lin 2003; Dullemond & Dominik 2004b). These investigations will be carried out in the future and presented elsewhere.

We wish to thank the anonymous referee for valuable comments. We thank to Dr. H. Tanaka for providing us with the single-sized monochromatic opacity table used in Tanaka et al. (2005). We are grateful to Drs P. Garaud and K. Kretke for useful conversation. This work is supported in part by NASA (NAGS5-11779, NNG04G-191G, NNG06-GH45G), JPL(1270927), NSF(AST-0507424, PHY99-0794), and Grant-in-Aid of the Japanese Ministry of Education, Science, and Culture (19540239).

A. Opacities

The Planck mean opacity is given by

$$\bar{\kappa}_j(T_{\text{rad}}) = \frac{\int_0^\infty \tilde{\kappa}_\nu(T_j) B_\nu(T_{\text{rad}}) d\nu}{\int_0^\infty B_\nu(T_{\text{rad}}) d\nu}, \quad (\text{A1})$$

where subscript j represents “s” (surface) or “m” (disk interior), ν is the frequency, $B_\nu(T_{\text{rad}})$ is the Planck function, and

$$\tilde{\kappa}_\nu(T_j) = \frac{\int_{s_{\text{min}}}^{s_{\text{max}}} \kappa_\nu(T_j, s) s^3 n(s) ds}{\int_{s_{\text{min}}}^{s_{\text{max}}} s^3 n(s) ds}. \quad (\text{A2})$$

Here $n(s) ds$ is the number density of grains with radii between s and $s + ds$, and the size distribution has the lower cutoff s_{min} and the upper cutoff s_{max} . In addition, $\kappa_\nu(T, s)$ is the single-sized (s) monochromatic (ν) dust opacity of grains with temperature T .

We assume a power-law size distribution $n(s) \propto s^{-3.5}$, which is truncated for a minimum and maximum range of $s_{\text{min}} = 0.1 \mu\text{m}$ and $s_{\text{max}} = 1 \text{mm}$.

The grain compositions and optical constants are adopted from Tanaka et al. (2005) and references therein. We use the resultant opacity table given by H. Tanaka. The table gives two single-sized monochromatic dust opacities as functions of ν and s : one for grains without ice or organics at high temperatures of $T > 160 \text{K}$ and the other for grains including ice or organics at $T < 160 \text{K}$.

B. Exact Solution of Dust Density Distribution

The gas density distribution ρ_g of the two-temperature model is given by

$$\rho_g(r, z) = \begin{cases} \rho_g(r, 0) \exp\left(-\frac{z^2}{2h^2}\right) & \text{if } |z| \leq z_s \\ \rho_g(r, z_s) \exp\left(-\frac{z^2 - z_s^2}{2H^2}\right) & \text{if } |z| \geq z_s, \end{cases} \quad (\text{B1})$$

where $h = c_m \Omega_K^{-1}$ (see eq. [5]) and $H = c_s \Omega_K^{-1}$ (c_s is the sound speed in the surface layer) are the gas scale height in disk interior and in the surface layer, respectively.

In a steady state, the sedimentation flux of the dust grains with their terminal velocity balances the diffusive mass flux due to gas turbulence (see eq. [30] in Takeuchi & Lin 2002) such that:

$$-\rho_d \Omega_K \hat{t}_{\text{stop}} z = \frac{\rho_g \nu}{\mathcal{S}c} \frac{\partial(\rho_d/\rho_g)}{\partial z}, \quad (\text{B2})$$

where \hat{t}_{stop} is the stopping time normalized by Ω_K^{-1} , ν is the turbulent viscosity, and $\mathcal{S}c$ is the Schmidt number representing coupling strength between grains and gas. The nondimensional stopping time \hat{t}_{stop} is given by

$$\hat{t}_{\text{stop}} = \frac{\rho_{\text{mat}} s \Omega_K}{\rho_g c_t}, \quad (\text{B3})$$

where ρ_{mat} is the material mass density, s is the dust radius, and c_t is the mean thermal velocity.

Solving equation (B2) with equations (B1) (in the case of $|z| \leq z_s$) and (B3), we obtain the dust density distribution of the disk interior to be (see eq. [31] in Takeuchi & Lin 2002)

$$\rho_{\text{dm}}(r, z) = \rho_{\text{dm}}(r, 0) \exp\left[-\frac{z^2}{2h^2} - \frac{\mathcal{S}c \hat{t}_{\text{stop},m}}{\alpha} \left(\exp \frac{z^2}{2h^2} - 1\right)\right], \quad (\text{B4})$$

where $\hat{t}_{\text{stop},m}$ is the stopping time in the midplane and $\alpha = \nu/(c_m h)$ is the non-dimensional turbulent viscosity in the so-called α -prescription (Shakura & Sunyaev 1973). The dimensionless stopping time in the midplane is given by

$$\hat{t}_{\text{stop},m} = \frac{\pi \rho_{\text{mat}} s}{2 \Sigma}. \quad (\text{B5})$$

The midplane dust density $\rho_{\text{dm}}(r, 0)$ is determined by the vertical integration of equation (B4) to be the surface density of dust $\Sigma_d = f_d \Sigma$, where f_d is the dust fraction in surface density.

Solving equation (B2) with equations (B1) (in the case of $|z| \geq z_s$) and (B3), we obtain the dust density distribution in the surface layer

$$\rho_{\text{ds}}(r, z) = \rho_{\text{dm}}(r, z_s) \exp\left[-\frac{z^2 - z_s^2}{2H^2} - \frac{\mathcal{S}c \hat{t}_{\text{stop},m} h}{\alpha H} \exp\left(\frac{z_s^2}{2h^2}\right) \left(\exp \frac{z^2 - z_s^2}{2H^2} - 1\right)\right], \quad (\text{B6})$$

where we put $\rho_{\text{ds}}(r, z_s) = \rho_{\text{dm}}(r, z_s)$ and assume that $\mathcal{S}c$ and α in the surface layer have the same values as those in the disk interior.

In the disk interior, dust sedimentation is not so important unless the radii of dust are not so large that we can formally set $\rho_{\text{dm}} = \rho_{\text{d}}$. In the surface layer, dust settling reduces the dust density while high surface temperature T_s raise it, so that ρ_{d} also gives a good estimate. Thus, instead of equations (B4) and (B6), we adopt, in most of the calculations, the simple density distribution given by equation (18).

C. The validity of the grazing-angle approximation

We derive the grazing-angle approximation (eq. [6]) and discuss its validity. Substituting $\rho_{\text{d}}(r, z)$ in equation (15) with that in equation (18) and assuming $A_s \ll 1$, we obtain

$$A_s = \tau_v \operatorname{erfc} \left(\frac{z_s}{\sqrt{2}h} \right) = \tau_v \operatorname{erfc} \left(\frac{\chi}{\sqrt{2}} \right), \quad (\text{C1})$$

where $\tau_v = \tilde{\kappa}_s(T_\star)\Sigma_{\text{d}}/2$ and $\chi = z_s/h$.

We derive the relation of A_s with a path integration from the star to the point (r, z) . Using equations (10) and (18), equation (9) can be written as

$$\tau_v(T_\star; r, z_s(r)) = \tau_v (1 + \zeta_s^2)^{1/2} \sqrt{\frac{2}{\pi}} \int_{R_\star}^r \frac{\hat{\Sigma}'_{\text{d}}}{h(r')} e^{-\chi'^2/2} dr' = 1 \quad (\text{C2})$$

with $\zeta_s = z_s/r$, $\hat{\Sigma}'_{\text{d}} = \Sigma_{\text{d}}(r')/\Sigma_{\text{d}}(r)$, and $\chi' = \zeta_s r'/h(r')$. Here we assume that $\bar{\kappa}_s(T_\star)$ is independent of position of the path. Substituting the integral variable from r' to χ' and noting that $\chi' \gg 1$ for $r' = R_\star$, we obtain

$$\tau_v (1 + \zeta_s^2)^{1/2} \zeta_s^{-1} \sqrt{\frac{2}{\pi}} \int_{\chi}^{\infty} \hat{\Sigma}'_{\text{d}} \left(\frac{d \ln \zeta'_h}{d \ln r'} \right)^{-1} e^{-\chi'^2/2} d\chi' = 1, \quad (\text{C3})$$

where we define $\zeta_h = h/r$ and $\zeta'_h = h(r')/r'$. Here we assume χ' is a monotonically increasing function with r' . From equations (C1) and (C3), we obtain

$$A_s = (1 + \zeta_s^2)^{-1/2} \zeta_s \left\langle \hat{\Sigma}'_{\text{d}} \left(\frac{d \ln \zeta'_h}{d \ln r'} \right)^{-1} \right\rangle_{g(\chi'), \chi}^{-1} \quad (\text{C4})$$

with

$$g(\chi') = \left[\operatorname{erfc} \left(\chi'/\sqrt{2} \right) \right]^{-1} \sqrt{2/\pi} \exp(-\chi'^2/2), \quad (\text{C5})$$

where $\langle X \rangle_{f(x'),x} = \int_x^\infty X(x')f(x') dx'$ represents the weighted average with a weight function $f(x')$.

If we substitute the Gaussian weight $g(\chi')$ with the delta function $\delta(\chi' - \chi)$ and assume $\zeta_s \ll 1$, we obtain

$$A_s = \zeta_s \left(\frac{d \ln \zeta_h}{d \ln r} \right). \quad (\text{C6})$$

Except for a small difference, this equation corresponds to equation (6). However, if the gradient $d \ln \zeta_h / d \ln r$ changes rapidly in r direction, the approximation used to derive equation (C6) is no longer justified. In this case A_s is determined not only by the local gradient of ζ_h but by the gradients in inner regions because the weight function $g(\chi')$ is extended to the inner radii. For this reason we use equations (9) and (15) instead of equation (C6).

REFERENCES

- Adams, F. C., Lada, C. J., & Shu, F. H. 1988, *ApJ*, 312, 788
- Chiang, E. I., & Goldreich, P. 1997, *ApJ*, 490, 368
- Chiang, E. I., Joungh, M. K., Creech-Eakman, M. J., Qi, C., Kessler, J. E., Blake, G. A., & van Dishoeck, E. F. 2001, *ApJ*, 547, 1077
- D'Alessio, P., Cantó, J., Hartmann, L., Calvet N., & Lizano, S. 1999, *ApJ*, 511, 896
- D'Alessio, P., Calvet N., Hartmann, L., Franco-Hernández & Servín, H. 2006, *ApJ*, 638, 314
- Dullemond, C. P. 2000, *A&A*, 361, L17
- Dullemond, C. P. & Dominik, C. 2004a, *A&A*, 417, 159
- Dullemond, C. P. & Dominik, C. 2004b, *A&A*, 421, 1075
- Dullemond, C. P., Dominik, C., & Natta, A. 2001, *ApJ*, 560, 957
- Furlan, E., et al. 2006 *ApJS*, 165, 568
- Gammie, C. F. 1996, *ApJ*, 457, 355
- Garaud, P., & Lin, D. N. C. 2007, *ApJ*, 654, 606
- Hayashi, C. 1981, *Prog. Theor. Phys. Suppl.*, 70, 35
- Kenyon, S. J., & Hartmann, L. 1987, *ApJ*, 323, 714

- Klahr, H. H. & Bodenheimer, P. 2003, *ApJ*, 582, 869
- Kusaka, T., Nakano, T., & Hayashi, C. 1970, *Prog. Theor. Phys. Suppl.*, 44, 1580
- Pollack, J. B., Hollenbach, D., Beckwith, S., Simonelli, D. P., Roush, T., & Fong, W. 1994, *ApJ*, 421, 615
- Shakura, N. I., & Sunyaev, R. A. 1973, *A&A*, 24, 337
- Takeuchi, T., & Lin, D. N. C. 2002, *ApJ*, 581, 1344
- Takeuchi, T., & Lin, D. N. C. 2003, *ApJ*, 593, 524
- Tanaka, H., Himeno, Y., & Ida, S. 2005, *ApJ*, 625, 414
- Watanabe, S., Nakagawa, Y., & Nakazawa, K. 1990, *ApJ*, 358, 282

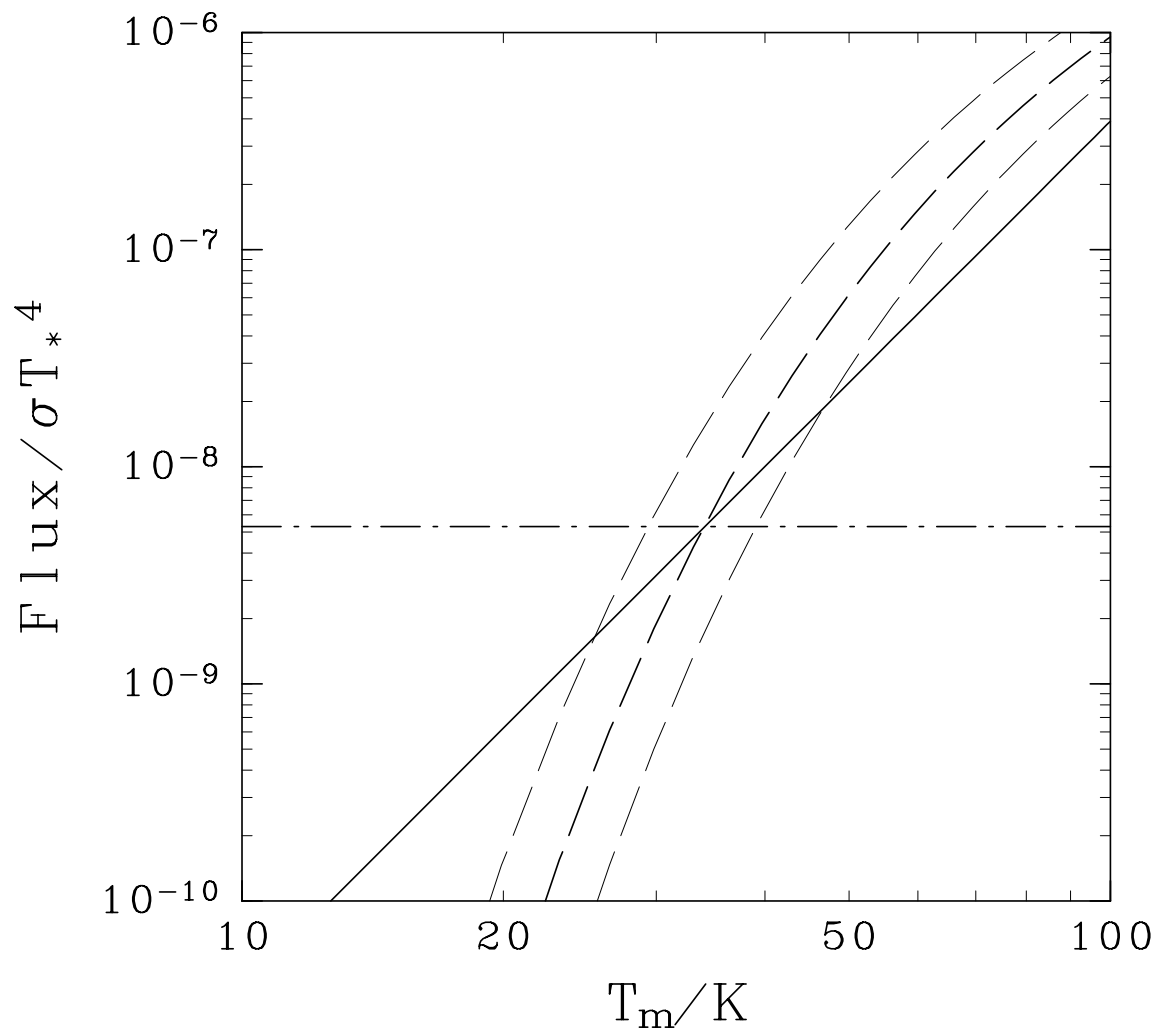


Fig. 1.— Disk thermal emission F_m (*solid line*) and intercepted stellar fluxes F_s at $r = 10$ AU with constant surface heights (*dashed curves*) of $z_s/r = 0.12$, 0.13 , and 0.14 (*left to right*) and with constant $\chi = z_s/h$ (*dot-dashed line*) as functions of disk temperature T_m . All fluxes are normalized by σT_*^4 .

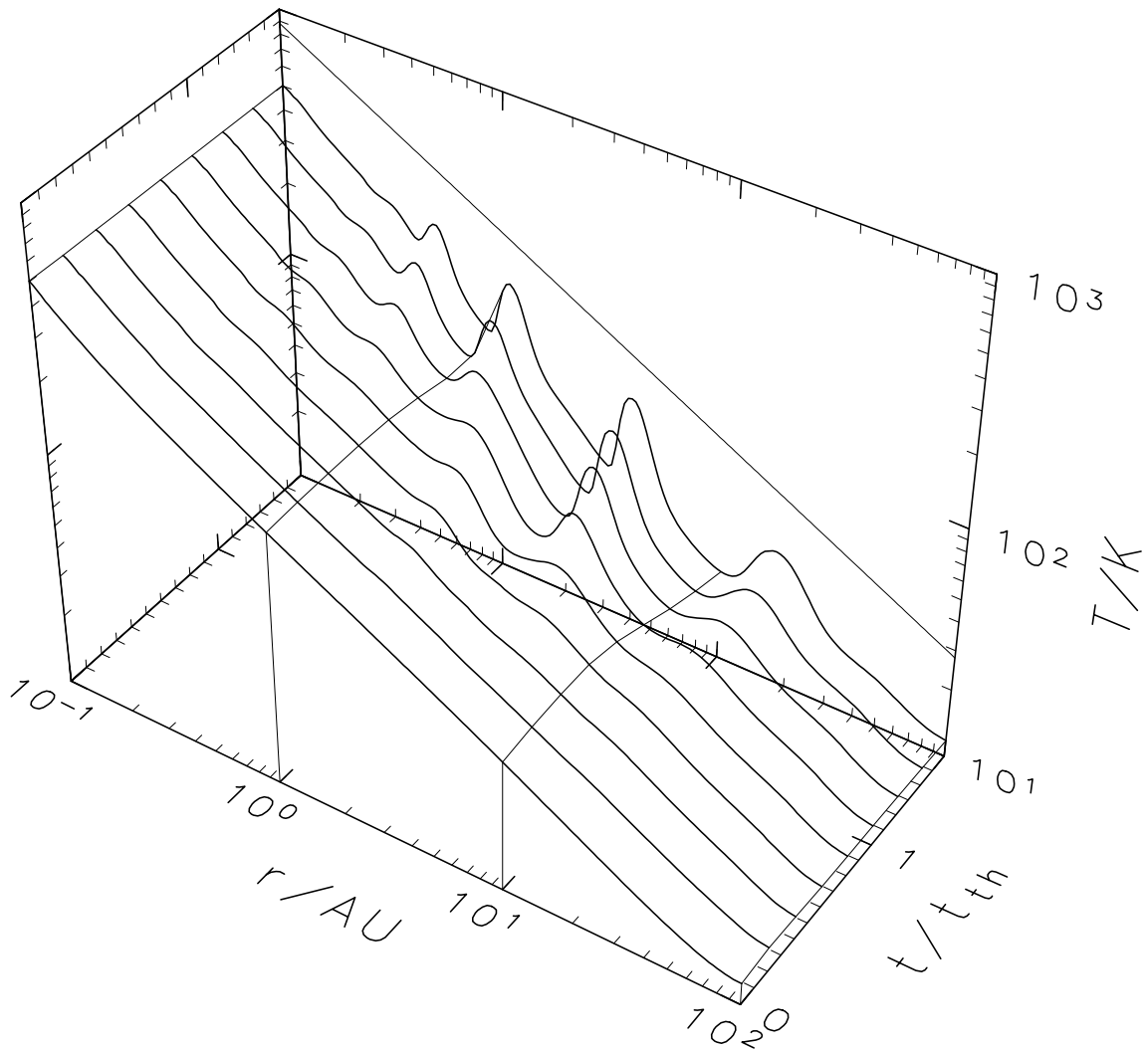


Fig. 2.— Initial stage of evolution of the midplane temperature T_m for the case of constant opacity and $\beta = 0$. The thick curves cover the range $\hat{t} = t/t_{\text{th},0} = 0.0$ – 1.6 with the interval $\Delta\hat{t} = 0.2$. The surface temperature T_s is represented by a thin line in the back panel. The surface density distribution is that prescribed by the MMSN model in which $p = 1.5$. The viscous dissipation associated with mass accretion is neglected (i.e., $\dot{M} = 0$).

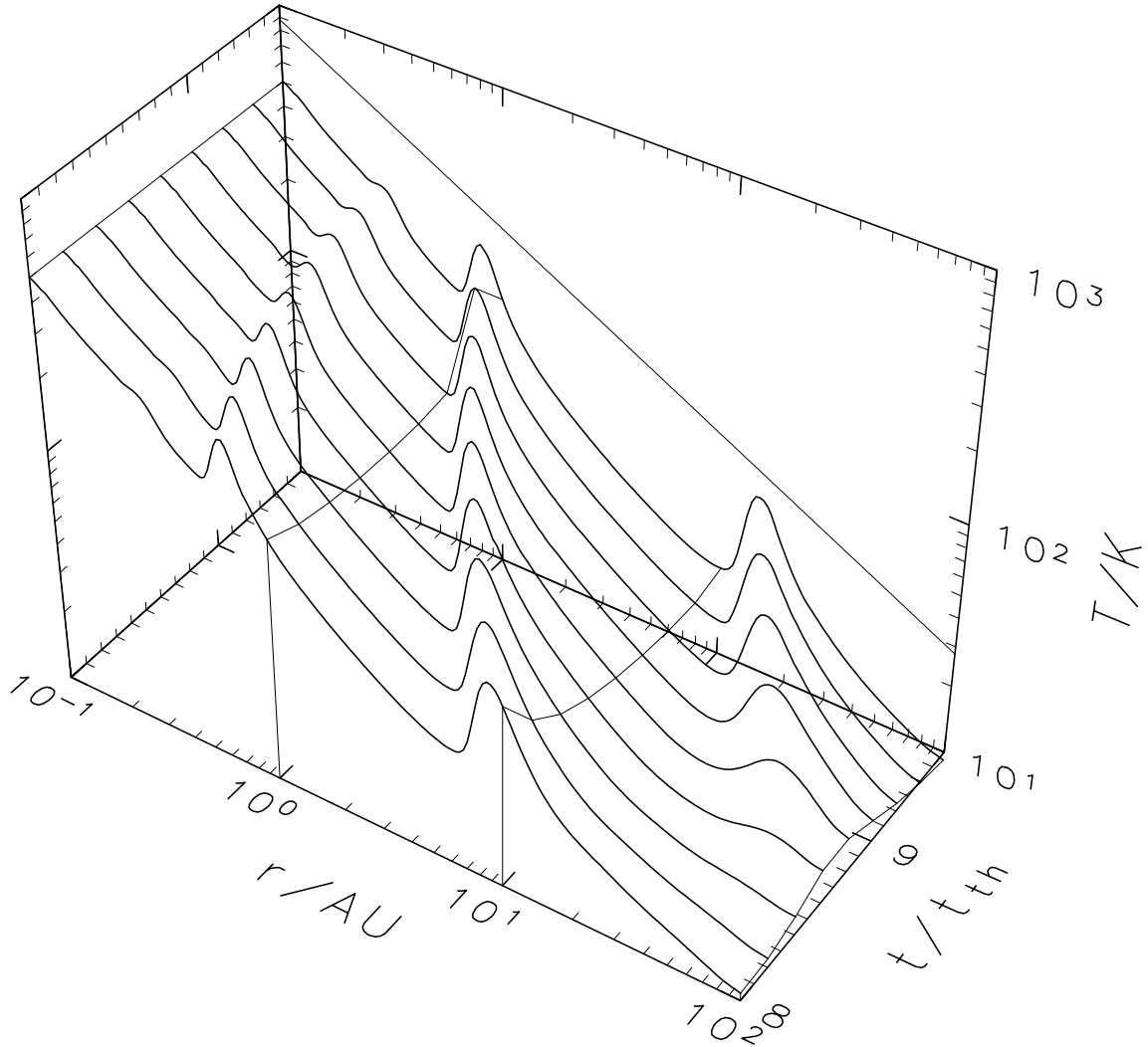


Fig. 3.— Time evolution of T_m after it has reached a quasi-periodic state. This model is the continuation of that shown in Fig. 2 to an epoch $\hat{t} = 8.0\text{--}9.6$. Each curve is separated by $\Delta\hat{t} = 0.2$. The T_s distribution is also shown in a thin line in the back panel. Other parameters are same as Fig. 2.

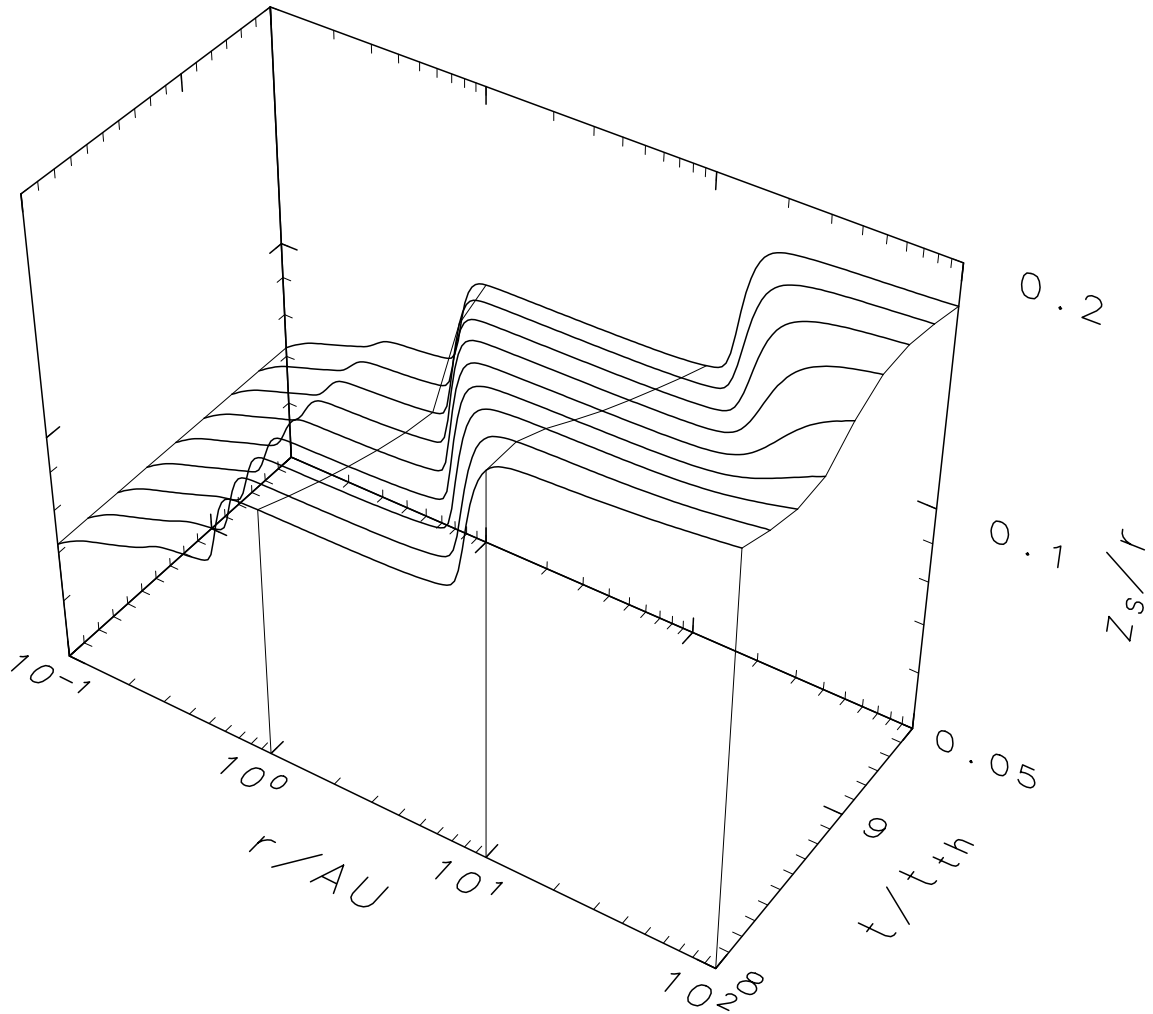


Fig. 4.— Time evolution of $\zeta_s = z_s/r$ in the quasi-periodic state at the same epoch as Fig. 3.

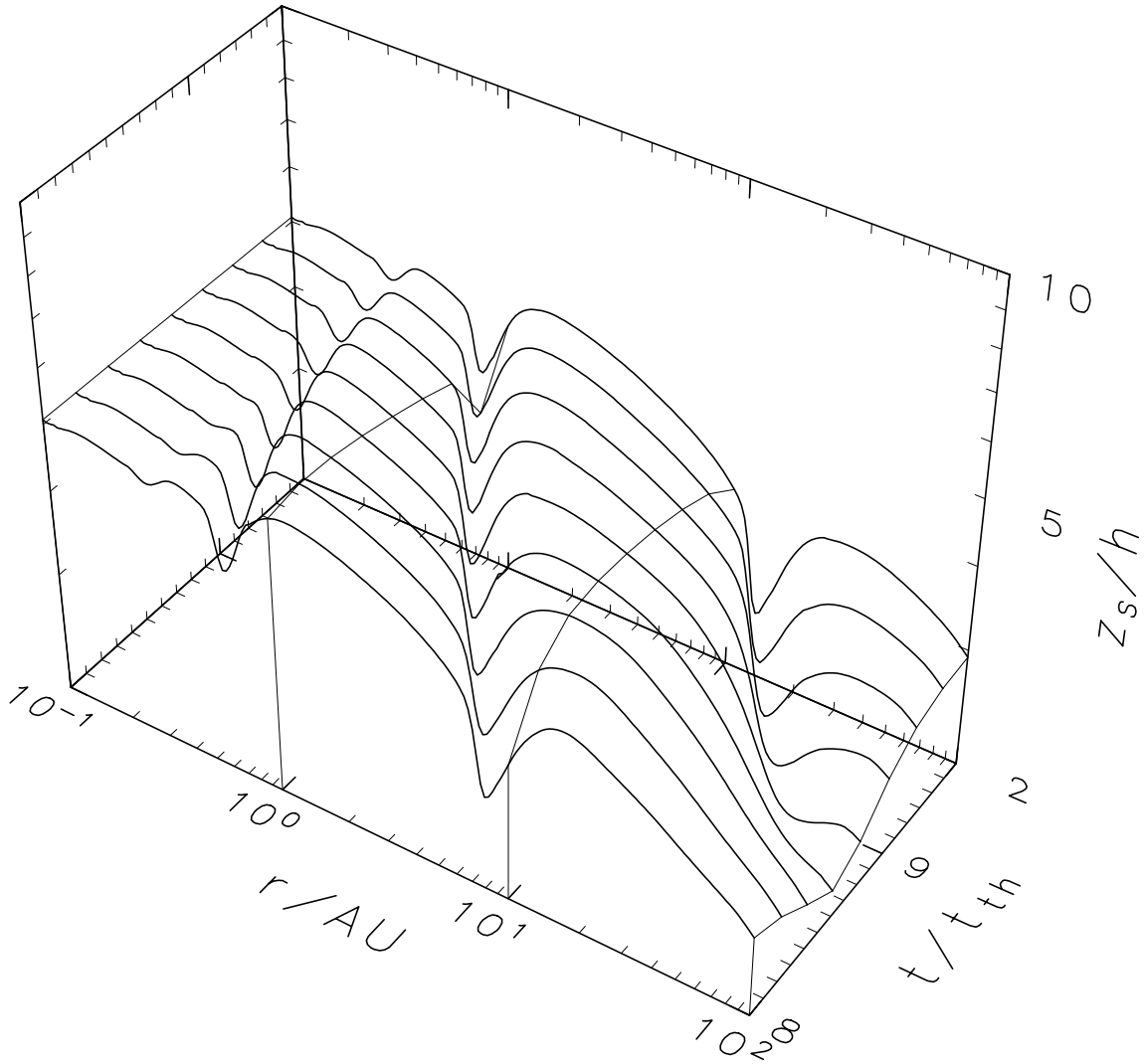


Fig. 5.— Time evolution of $\chi = z_s/h$ in the quasi-periodic state at the same epoch as Fig. 3.

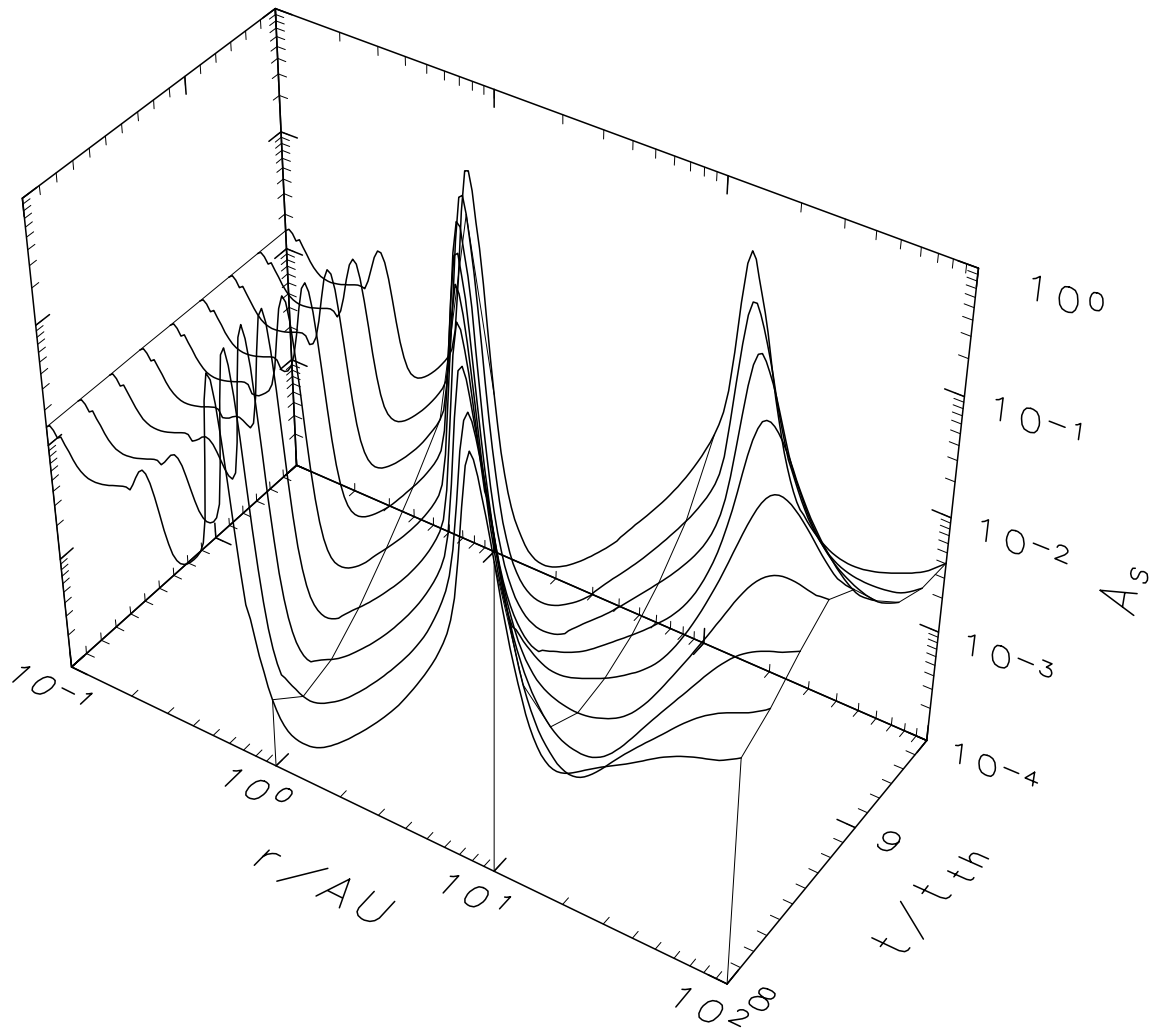


Fig. 6.— Time evolution of surface filling factor A_s in quasi-periodic state at the same epoch as Fig. 3.

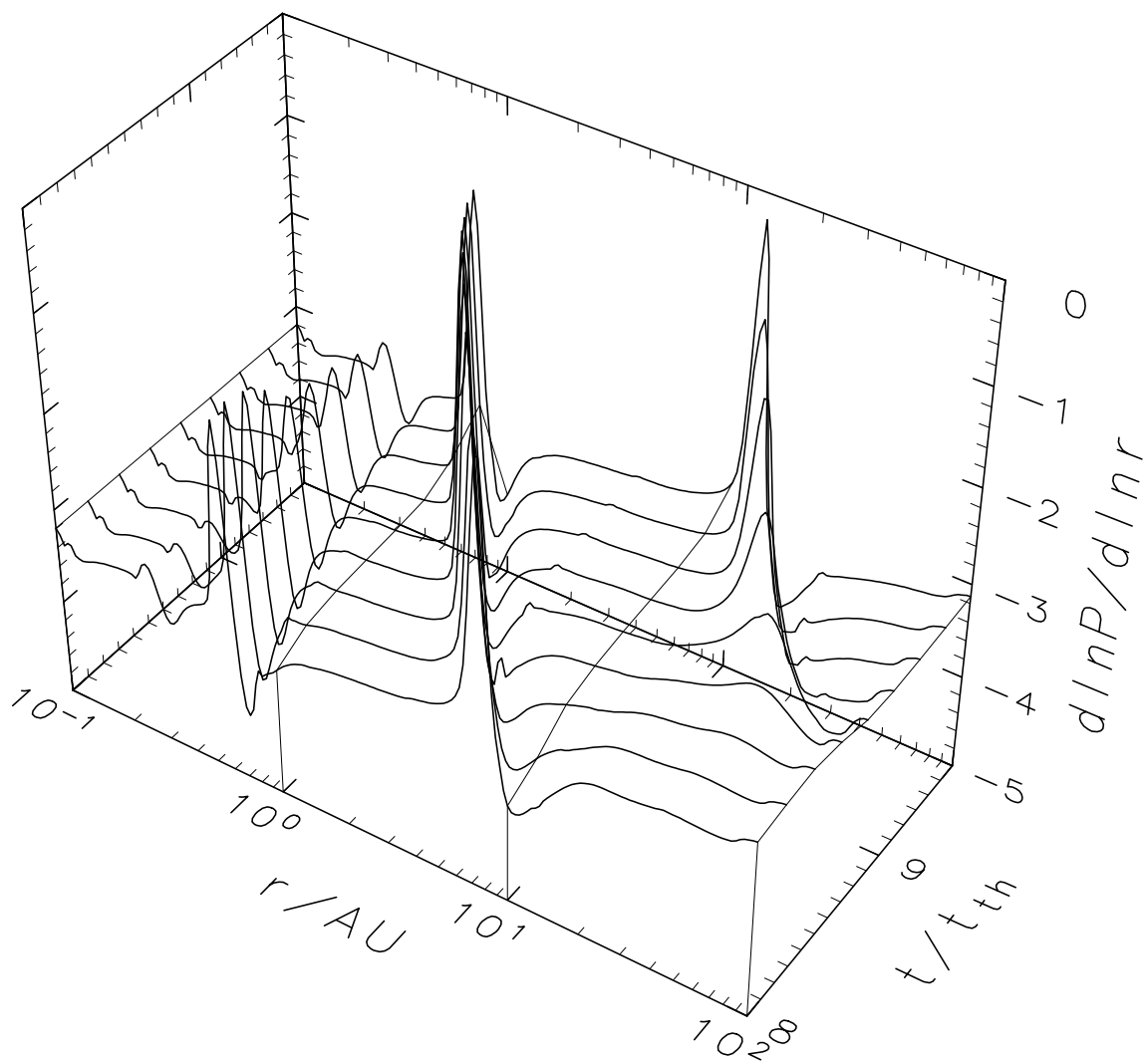


Fig. 7.— Time evolution of the logarithmic pressure gradient $d \ln P / d \ln r$ in quasi-periodic state at the same epoch as Fig. 3.

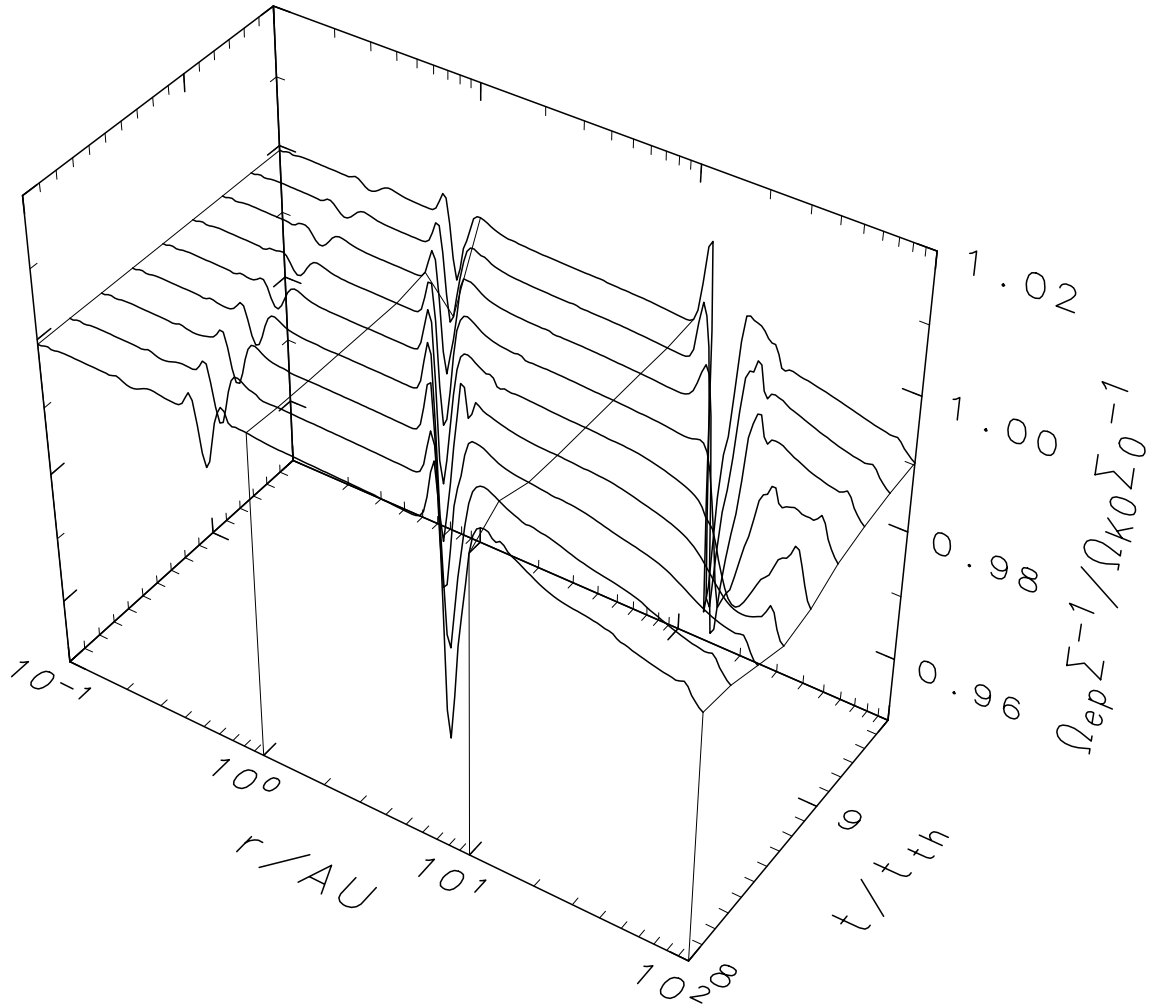


Fig. 8.— Time evolution of potential vorticity $\Omega_{ep}\Sigma^{-1}$ normalized by the Keplerian value at 1 AU ($\Omega_{K0}\Sigma_0^{-1}$) in quasi-periodic state at the same epoch as Fig. 3.

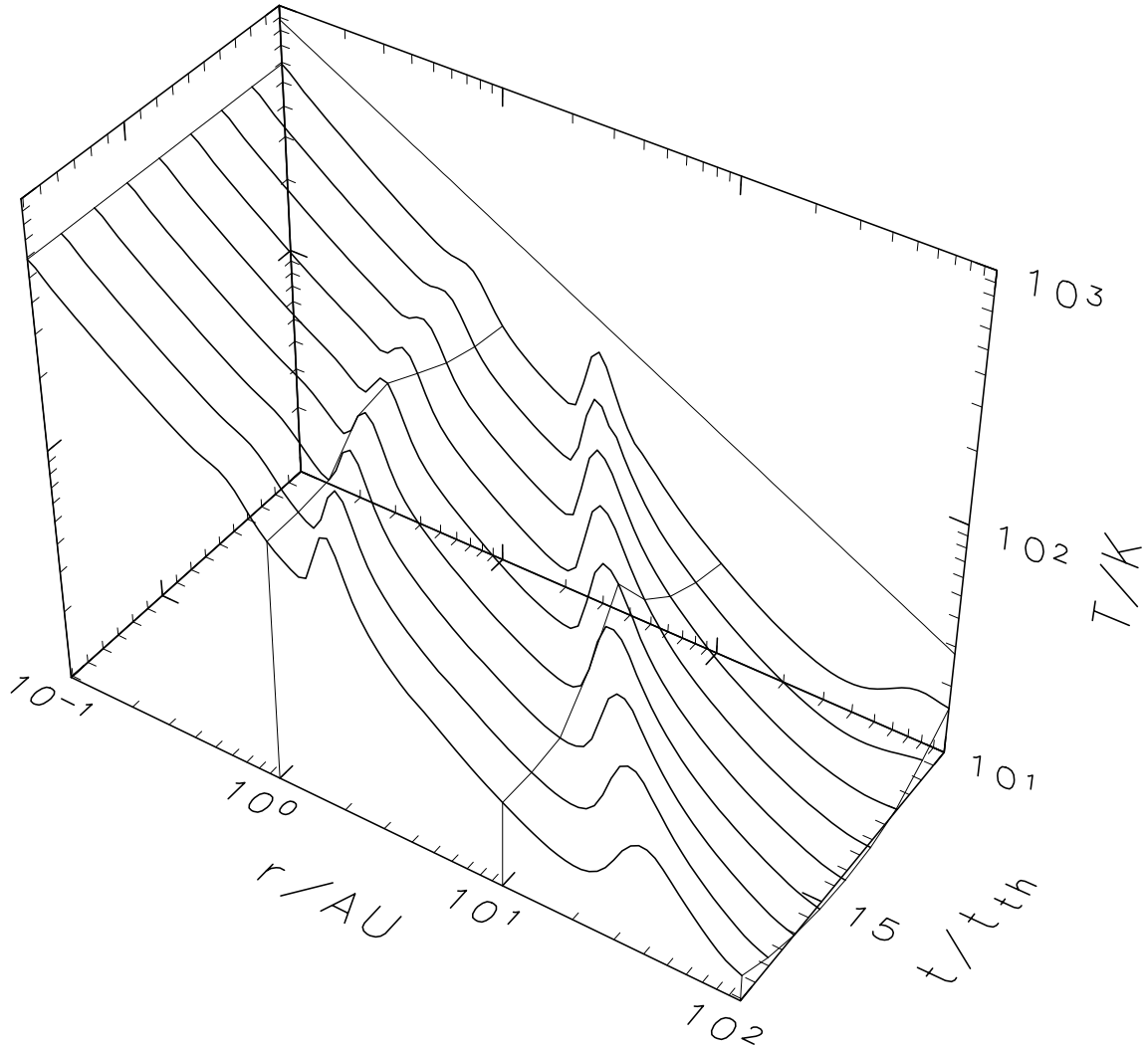


Fig. 9.— Quasi-periodic evolution of T_m for steady accretion disk with $\dot{M} = 10^{-8} M_{\odot} \text{yr}^{-1}$ (at $\hat{t} = 14.4\text{--}16.0$ with $\Delta\hat{t} = 0.2$). The distribution of T_s is also shown with a thin solid line in the back panel. Other parameters are same as Fig. 3.

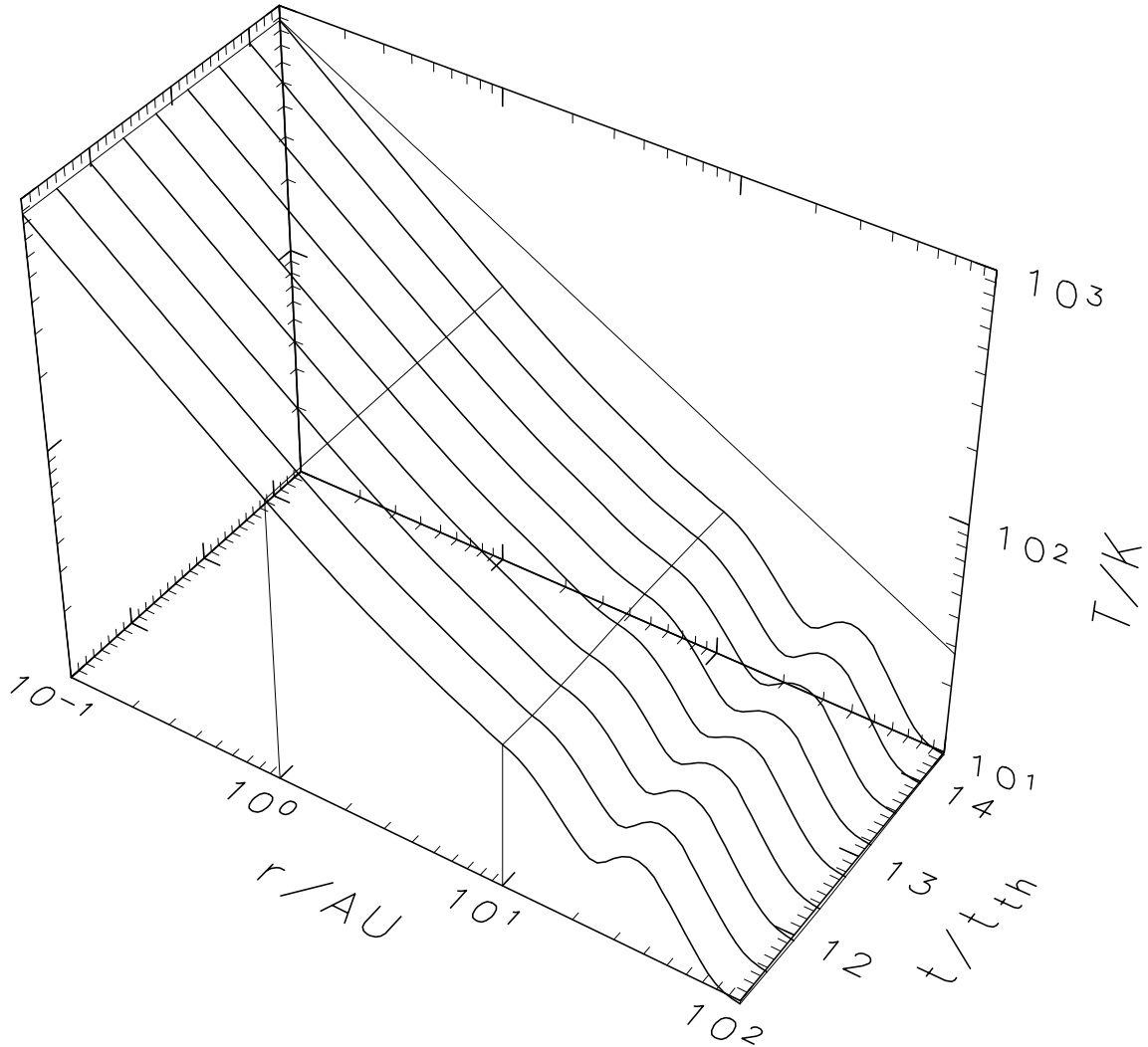


Fig. 10.— Quasi-periodic evolution of T_m for steady accretion disk with $\dot{M} = 10^{-7} M_{\odot} \text{yr}^{-1}$ ($\hat{t} = 11.2\text{--}14.4$ with $\Delta\hat{t} = 0.4$). The distribution T_s is also shown with a thin solid line in the back panel. Other parameters are same as Fig. 3.

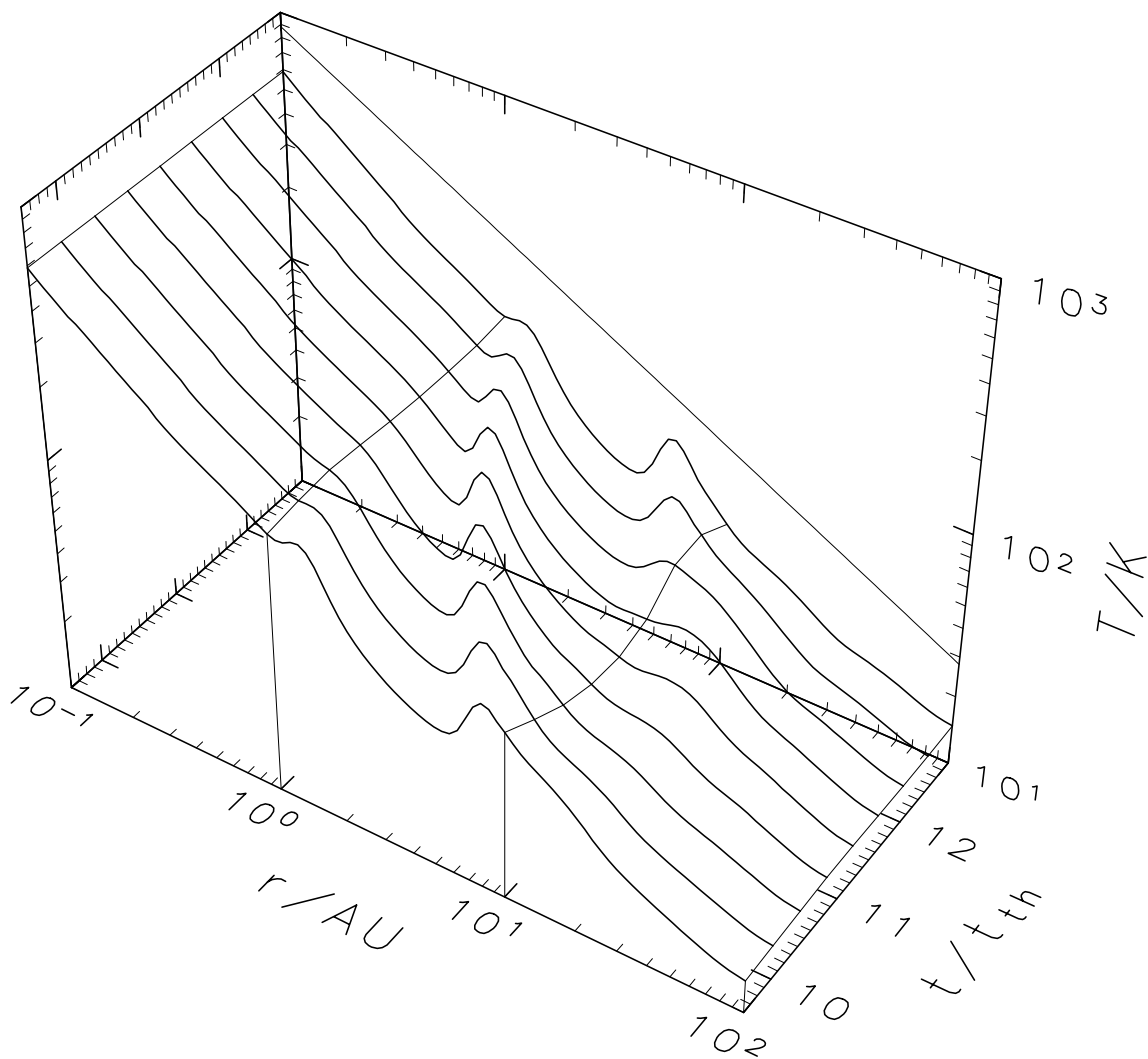


Fig. 11.— Quasi-periodic evolution of T_m for a steady accretion disk with $p = 1.0$ and $\dot{M} = 10^{-8} M_\odot \text{yr}^{-1}$ ($\hat{t} = 9.6\text{--}12.8$ with $\Delta\hat{t} = 0.4$). The distribution of T_s is also shown with a thin solid line in the back panel. Opacities are same as Fig. 3.

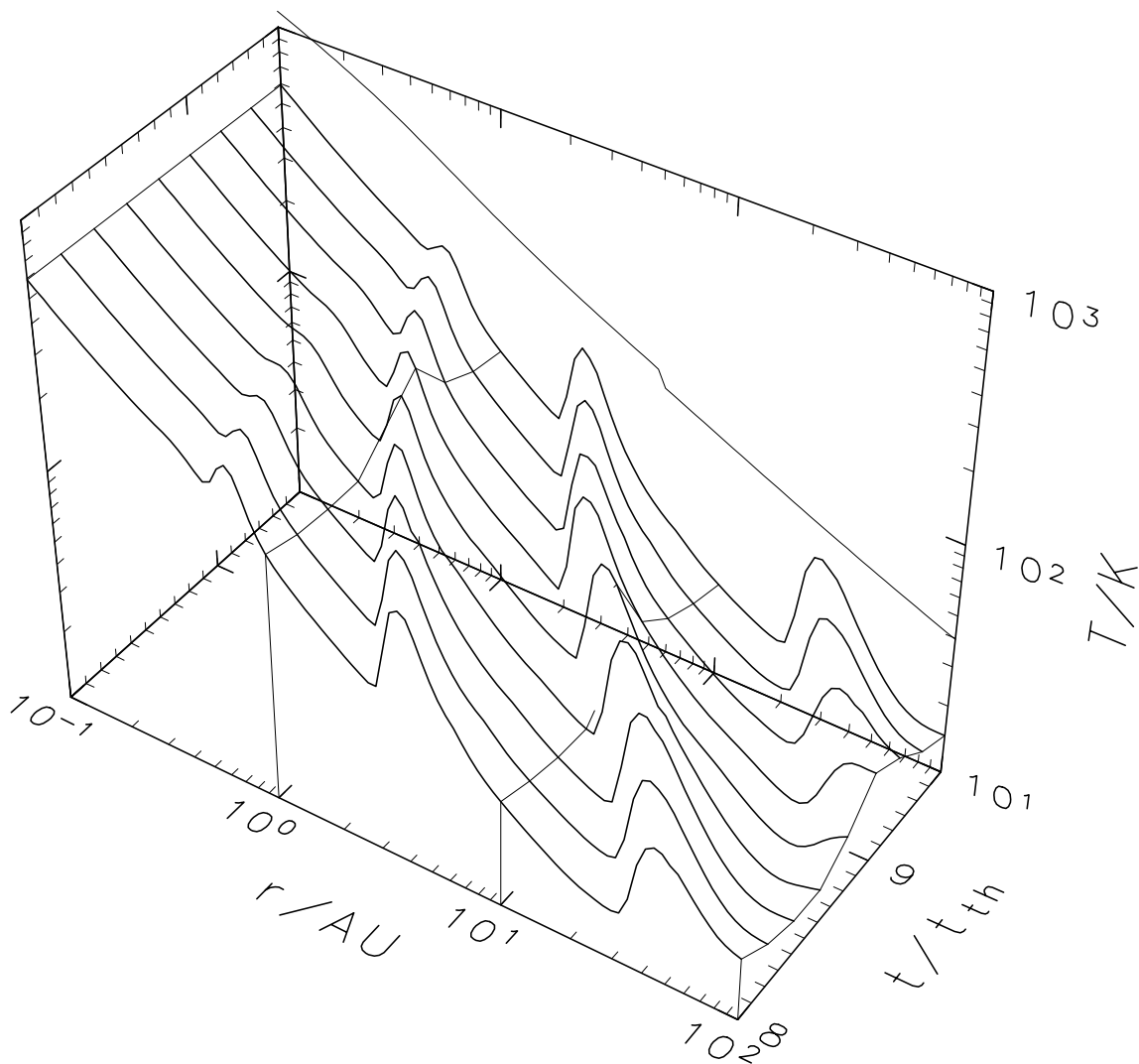


Fig. 12.— Quasi-periodic evolution of T_m for realistic opacities as well as T_s (a thin solid line in the back panel). The disk structural parameters is that of a MMSN model ($p = 1.5$) with steady $\dot{M} = 10^{-8} M_\odot \text{yr}^{-1}$. The opacity law changes at 160 K but the effect of ice sublimation is neglected. Maximum size of surface dust grains is assumed to be 1 mm (same as that in disk interior). Times are same as Fig. 3.

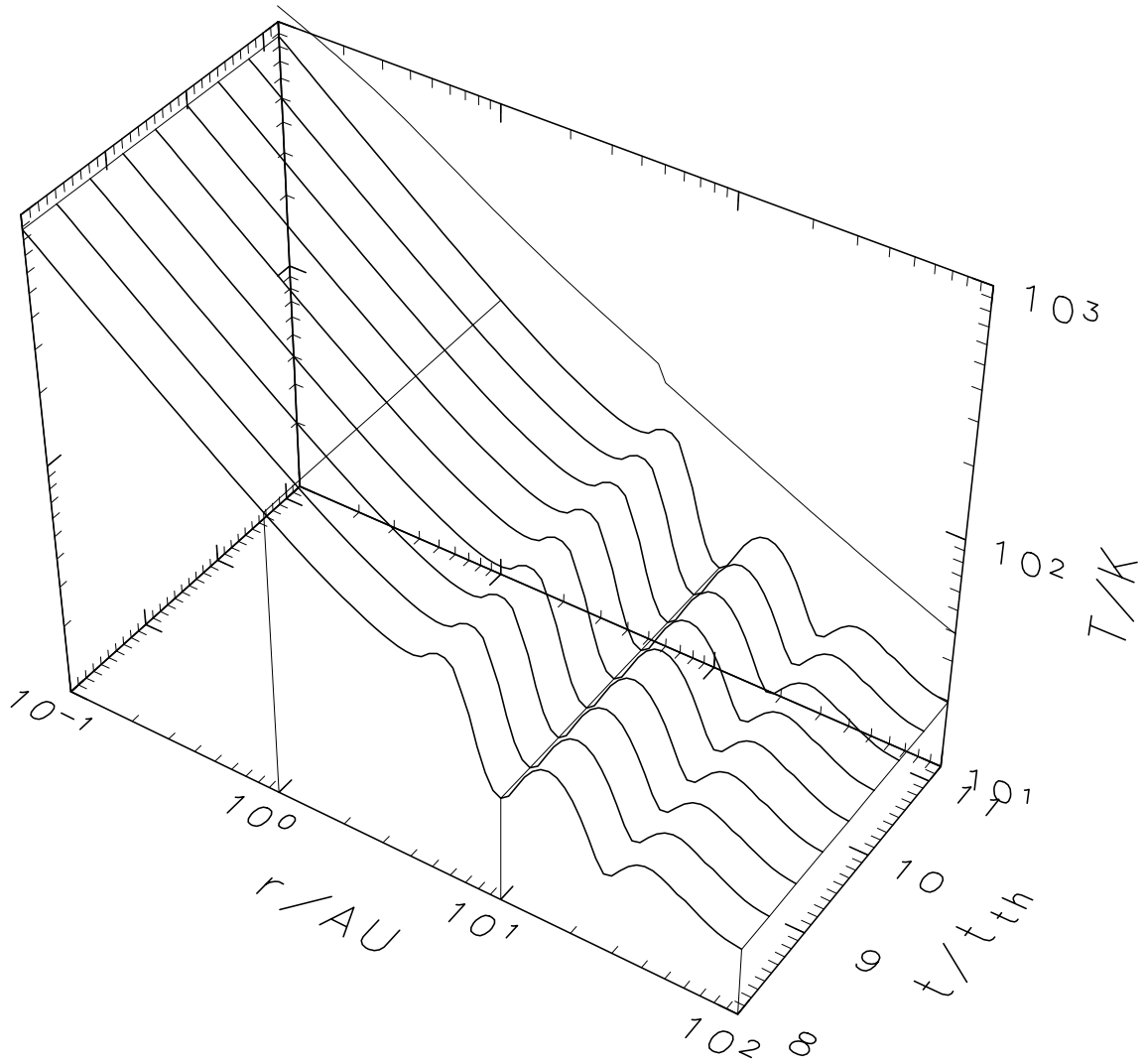


Fig. 13.— Same as Fig. 12, but for a disk with $\dot{M} = 10^{-7} M_{\odot} \text{yr}^{-1}$ and $\hat{t} = 8.0\text{--}11.2$ with $\Delta\hat{t} = 0.4$.

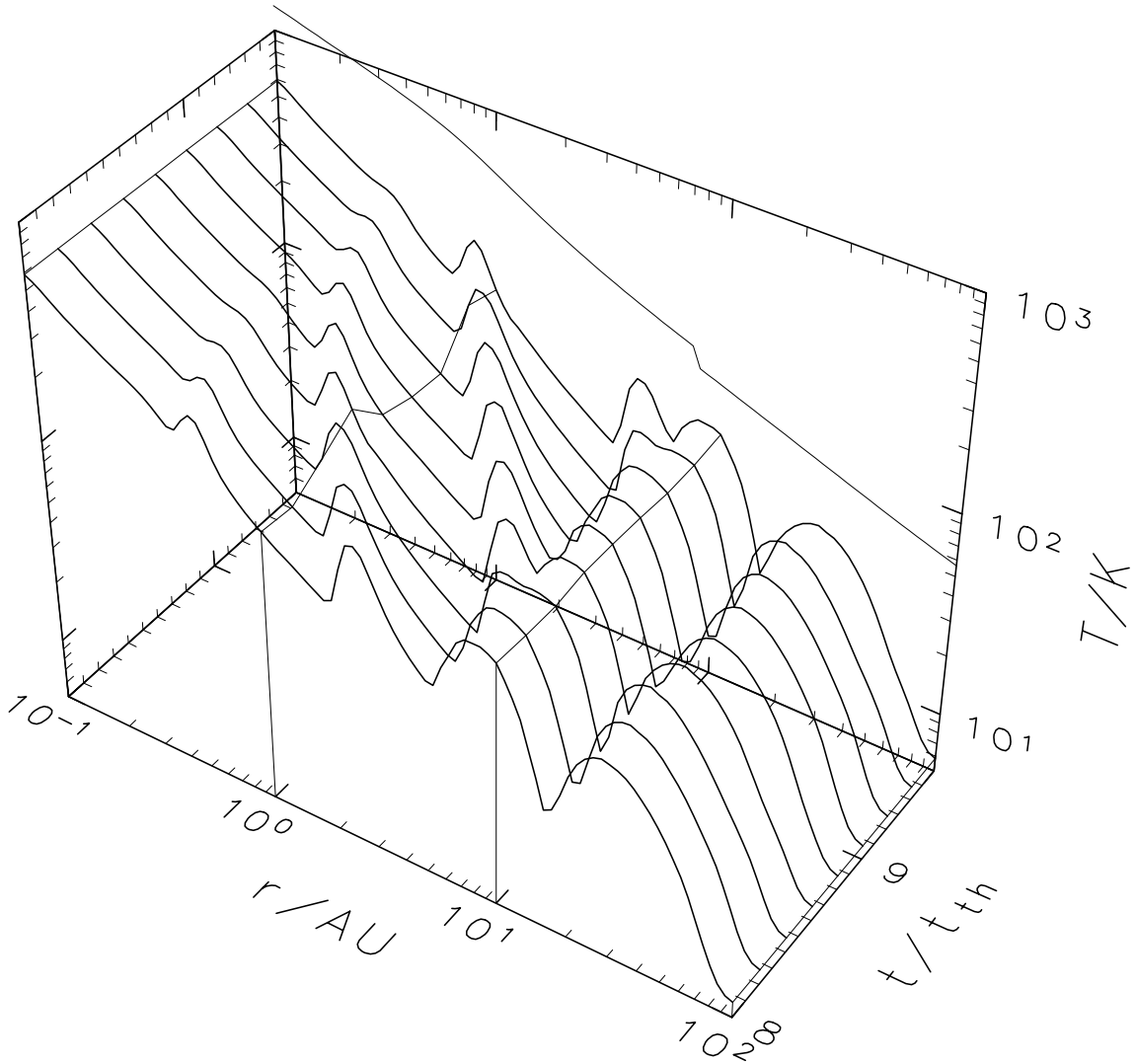


Fig. 14.— Same as Fig. 12, but taking into account the effect of ice sublimation. The maximum size of surface dust grains is reduced to $1\ \mu\text{m}$.

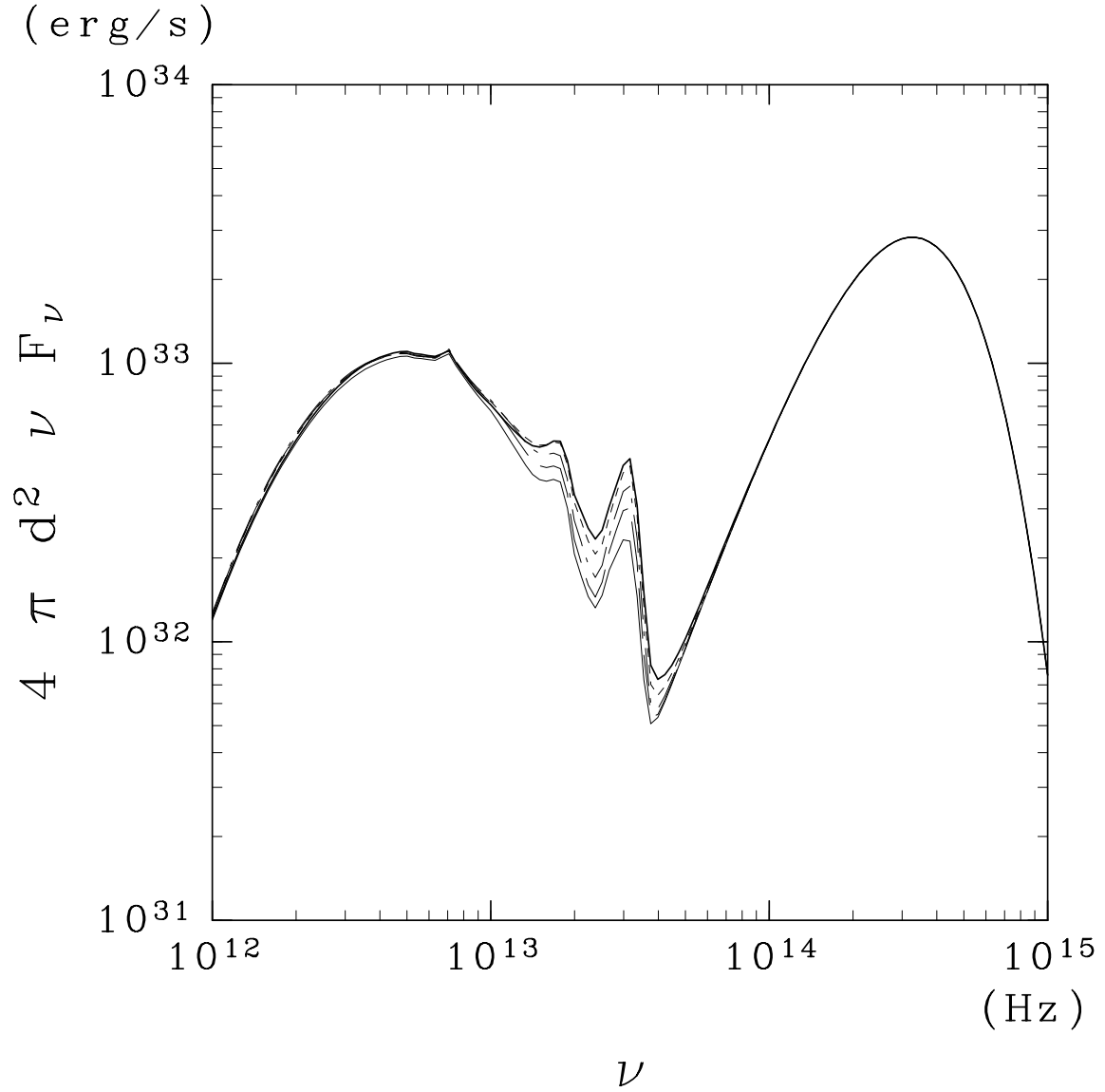


Fig. 15.— Quasi-periodic change of SED calculated from the model shown in Fig. 14. Different lines represent the epochs $\hat{t} = 8.4$ (*thick solid curve*), 8.6 (*thin solid curve*), 8.8 (*dashed curve*), 9.0 (*dash-dotted curve*), 9.2 (*dotted curve*), and 9.4 (*thick solid curve, coincide with that at $\hat{t} = 8.4$*), respectively. Note that $t = 53\hat{t}$ yr.